LUND UNIVERSITY

Transmission Electron Microscopy of Nanowires: Influence of Doping and Etching on Polytypism in InP

Ek, Martin

2011

Link to publication

Citation for published version (APA):
Ek, M. (2011). *Transmission Electron Microscopy of Nanowires: Influence of Doping and Etching on Polytypism in InP*. [Licentiate Thesis, Centre for Analysis and Synthesis]. Lund University.

Total number of authors:
1

General rights
Unless other specific re-use rights are stated the following general rights apply:
Copyright and moral rights for the publications made accessible in the public portal are retained by the authors and/or other copyright owners and it is a condition of accessing publications that users recognise and abide by the legal requirements associated with these rights.
• Users may download and print one copy of any publication from the public portal for the purpose of private study or research.
• You may not further distribute the material or use it for any profit-making activity or commercial gain
• You may freely distribute the URL identifying the publication in the public portal

Read more about Creative commons licenses: https://creativecommons.org/licenses/

Take down policy
If you believe that this document breaches copyright please contact us providing details, and we will remove access to the work immediately and investigate your claim.

LUND UNIVERSITY

PO Box 117
221 00 Lund
+46 46-222 00 00

Transmission Electron Microscopy of Nanowires: Influence of Doping and Etching on Polytypism in InP

Martin Ek

Licentiate thesis

2011

LUND
UNIVERSITY

Polymer & Materials Chemistry
Centre for Analysis and Synthesis
Sweden

Avhandlingen presenteras vid ett offentligt seminarium den 19 december 2011 kl. 14.15
i hörsal G på Kemicentrum, Lund

Polymer & Materials Chemistry
Centre for Analysis and Synthesis
Lund University
P.O. Box 124
SE-221 00 Lund
Sweden

© Martin Ek
ISBN 978-91-7422-290-6
Printed by Media-Tryck, Lund
December 2011

Abstract

Semiconductor nanowires have many properties which makes them interesting for future electronic devices. The fact that they have very small diameters allow them to combine different III-V materials into heterostructures, and makes it possible to grow them on Si substrates which are the basis of nearly all current semiconductor technology. It also allows them to adopt the wurtzite crystal structure in addition to the zincblende, which is the bulk form (except for III-nitrides).

The small dimensions of the nanowires mean that there is a need for high resolution analysis of both crystal structure and composition locally. For this purpose transmission electron microscopy (TEM) is an excellent tool: crystal structure can be directly viewed using high resolution imaging and the electrons passing through the sample generate many signals, among them X-rays, which can be used for compositional analysis.

In this thesis the effects of doping (with Zn and S) and etching (with HCl) on the nanowire crystal structure are analysed using high resolution TEM. These are procedures which will be essential in many device applications. To know the exact atomic arrangement at the interface between two crystal structures, higher resolution than is obtainable in conventional TEM is required. For this purpose a combination of hardware aberration corrected TEM and focal series reconstruction was used.

Contents

List of papers **v**

1 Introduction **1**
1.1 Nanowires 1
1.2 Electron microscopy 2

2 Transmission Electron Microscopy **5**
2.1 The intrument 6
2.2 High resolution imaging 8
2.3 Correction of lens aberrations 15
2.4 TEM image simulation 19
2.5 Scanning transmission electron microscopy 20
2.6 Energy dispersive X-ray spectroscopy 20

3 Nanowires **23**
3.1 Growth 23
3.2 Crystal structure 25
3.3 Additional steps during growth: doping and etching 28

4 Results **33**
4.1 Changes in crystal structure with doping and etching 33
4.2 Twin interface structure 39
4.3 Outlook 42

Acknowledgements **43**

References **45**

List of papers

This thesis is based on the following papers, which will be referred to in the text by Roman numerals.

I
Electron Image Series Reconstruction of Twin Interfaces in InP Superlattice Nanowires
Martin Ek, Magnus T. Borgström, Lisa S. Karlsson, Crispin J.D. Hetherington, L. Reine Wallenberg
Microscsopy and Microanalysis **17** (2011) 752

II
Changes in Contact Angle of Seed Particle Correlated with Increased Zincblende Formation in Doped InP Nanowires
Jesper Wallentin, Martin Ek, L. Reine Wallenberg, Lars Samuelson, Knut Deppert, Magnus T. Borgström
Nano Letters **10** (2010) 4807

III
Probing the Wurtzite Conduction Band Structure Using State Filling in Highly Doped InP Nanowires
Jesper Wallentin, Kilian Mergenthaler, Martin Ek, L. Reine Wallenberg, Lars Samuelson, Knut Deppert, Mats-Erik Pistol, and Magnus T. Borgström
Nano Letters **11** (2011) 2289

IV
In Situ Etching for Total Control Over Axial and Radial Nanowire Growth
Magnus T. Borgström, Jesper Wallentin, Johanna Trägårdh, Peter Ramvall, Martin Ek, L. Reine Wallenberg, Lars Samuelson, Knut Deppert
Nano Research **3** (2010) 264

My contributions

I
In this paper we use focal series reconstruction to remove the effects of the lens aberrations from the images in order to enable full atomic resolution of the twin interfaces in an InP nanowire. I acquired the TEM focal series together with Crispin Hetherington on an aberration corrected 200 kV microscope. I performed the simulations used to match the different possible interface structures with the reconstructed object wavefunction. I was the main author for the paper.

II
I performed the TEM characterization and did the statistical analysis of the crystal structure. I also performed the compositional analysis using STEM and XEDS.

III
I performed the TEM characterization and did the statistical analysis of the crystal structure. I also performed the compositional analysis, including the radial distribution of S in the nanowires, using STEM and XEDS.

IV
I performed the TEM characterization and did the analysis of the crystal structure.

Papers not included in the thesis:
I contributed to these papers which are outside the scope of this thesis.

V
Valence Band Splitting in Wurtzite InP Nanowires Observed by Photoluminescence and Photoluminescence Excitation Spectroscopy
Gerben L. Tuin, Magnus T. Borgström, Johanna Trägårdh, Martin Ek, L. Reine Wallenberg, Lars Samuelson and Mats-Erik Pistol
Nano Research **4** (2011) 159

VI
High Current Density Esaki Tunnel Diodes Based on GaSb-InAsSb Heterostructure Nanowires
Bahram Ganjipour, Anil W. Dey, Mattias B. Borg, Martin Ek, Mats-Erik Pistol, Kimberly A. Dick, Lars-Erik Wernersson, and Claes Thelander
Nano Letters **11** (2011) 4222

VII
Formation of the axial heterojunction in GaSb/InAs(Sb) nanowires with high crystal quality
Martin Ek, Mattias B. Borg, Anil W. Dey, Bahram Ganjipour, Claes Thelander, Lars-Erik Wernersson, and Kimberly A. Dick
Crystal Growth & Design **11** (2011) 4588

VIII
InAs quantum dots and quantum wells grown on stacking-fault controlled InP nanowires with wurtzite crystal structure
Kenichi Kawaguchi, Magnus Heurlin, David Lindgren, Magnus T. Borgström, Martin Ek, and Lars Samuelson
Applied Physics Letters **99** (2011) 131915

IX
Diameter Reduction of Nanowire Tunnel Heterojunctions using In-Situ Annealing
B. Mattias Borg, Martin Ek, Kimberly A. Dick, Bahram Ganjipour, Anil W. Dey, Claes Thelander, and Lars-Erik Wernersson
Applied Physics Letters **99** (2011) 203101

Chapter 1

Introduction

1.1 Nanowires

Nanowires are materials designed to have two dimensions in the nanometre size range (usually between 10 nm to a few hundred nanometres) while being much larger in the third (hundreds of nanometres to several micrometres). Most nanowire synthesis methods can be described as bottom-up where the material spontaneously forms the desired shape, in contrast to top-down methods using masks and etches to carve out the structure. For semiconductor materials the nanowire geometry offers several advantages, for instance if the diameter is made small enough the nanowire will essentially be a 1D object allowing access to ballistic transport phenomena. Perhaps less obvious, but just as important, is the fact that having a small diameter allows the nanowire to accommodate lattice mismatched materials very efficiently by radial relaxation of the strain.[1] This allows the creation of heterostructures of two different materials with defect free interfaces which would have formed dislocations if attempted in planar growth.[2]

III-V semiconductors, containing one group III and one group V element, are one class of materials that have been successfully grown as nanowires, allowing a wide choice of different band-gaps (and accordingly different lattice parameters). In this fashion several working electronic devices have already been manufactured, such as diodes [3, 4] and transistors[5, 6]. The ability to combine lattice mismatched materials has also made it possible to grow nanowires made of III-V materials on Si wafers, offering a route to integrating these high performance materials for special applications with Si based planar devices [7, 8]. This is essential as the technology for Si devices is well established, well developed and forms the basis of the current semiconductor industry.

One interesting side effect of the way the III-V nanowires are grown is that they do not necessarily adopt the same crystal structure as their bulk counterparts: most III-V materials have a cubic zincblende structure in bulk but in nanowires they can also form the hexagonal wurtzite structure. Often the nanowires are not purely one or the other

but contain a mix of the two, or have twins or stacking faults. If this occurs in an uncontrolled manner it can be detrimental to the properties of the nanowire,[9, 10] but if controlled by careful tuning of the growth it offers the possibility of modifying the band structure without changing the material.[11, 12] The crystal structure can also be affected by the addition of dopant precursors during the nanowire growth, which forms the basis for paper II and III.

The basics of III-V semiconductor nanowire growth and crystal structure are briefly discussed in *chapter 3* in order to provide a background for the microscopy characterization techniques which are the focus of this thesis.

1.2 Electron microscopy

Of course the small size of the nanowires (or indeed any modern electronic device) demands analysis methods with very high resolution and sensitivity in order determine their morphology, crystal structure and composition; only then is it possible to connect the growth conditions with the performance of the material. The various transmission electron microscopy (TEM, used both for the instrument and the method) techniques are discussed in *chapter 2*.

The resolution of a microscope, i.e. the minimum distance between two separate points in the object where they are imaged as such and not blurred into a single feature, is comparable to the wavelength of the illumination used. Typical electron wavelengths used in high resolution TEM are on the order of 0.002 nm, much smaller than the interatomic distances in crystals which are around 0.2 nm. Electrons have a large advantage over photons in this regard as it is possible to construct magnetic lenses which work even for very short wavelengths; in contrast the glass lenses used in visible light microscopes are useless for X-rays (which would be required to form images with atomic resolution). One might therefore think that it would be no problem to directly image the crystal structure and to resolve all the atomic positions, but unfortunately the magnetic lenses cause distortions in the images which impose a much harsher limit on resolution than does the illumination wavelength. *Section 2.2* offers a more detailed description of imaging and resolution.

The aberrations in the magnetic lenses which cause the distortions in the images can be compensated using additional lenses (hardware aberration correction), post processing of the images (software aberration correction) or a combination of both.[13] These methods, described in *section 2.3*, extend the resolution enough to give truly atomic resolution images, enabling more detailed characterization of the crystal structure, for instance at twin boundaries as detailed in paper I.

Electrons interact strongly with the object as they pass through it in the microscope. By analysing the X-rays that are generated by these interactions or by measuring the amount of energy lost by the electron it is possible to also do compositional anal-

ysis of the sample (see *section 2.6*). Correlated with the crystal structure information from the images, this makes the TEM a very powerful instrument for characterization of materials. Unfortunately this strong interaction also has the consequence that the sample can be damaged by the illumination and that the contrast in the images is very sensitive to sample thickness, adding an additional complication to their interpretation. Comparisons between the acquired images and simulations should therefore be used to verify any detailed analysis. Simulated images where used for this purpose in paper I and the method is outlined in *section 2.4*.

Chapter 2

Transmission Electron Microscopy

The main topic of this thesis is transmission electron microscopy techniques dealing with high resolution imaging. Before the aberration correction methods used to extend the resolution of TEM are discussed, some background on how images are formed in conventional high resolution TEM (HRTEM) is needed. The theory behind image formation forms the framework for not only aberration correction, but also for aberration measurement and image simulation. For the concepts in image formation to be meaningful, some general background on the workings of a TEM is also provided. The two microscopes used in this thesis, the 300 kV JEOL 3000F at nCHREM in Lund and the 200 kV aberration corrected JEOL 2200MCO at the department of Materials in Oxford, are used as examples.

Contrast, the relative difference in intensity between two areas (or individual pixels), is a very important concept in microscopy. The description of imaging in HRTEM and the limits to resolution from lens aberrations and microscope instabilities are all described in terms of how the contrast is reduced for different periodicities in the image. If the contrast is reduced to zero for some sufficiently small separation of two objects, then they cannot be resolved simply because there is no contrast to distinguish one from the other.

When talking about resolution it can be useful to put the numbers in relation to some actual interatomic distances in the material we are interested in. For example, if the resolution is better than 0.34 nm it is possible to resolve the (111) planes in InP, which makes the wurtzite and zincblende crystal structures distinguishable from each other. For InP this could be said to be the minimum resolution where the term high resolution TEM is warranted. If the resolution is improved to better than 0.15 nm even the shortest In-P distances in the $\langle 110 \rangle$ projection can be resolved, enabling full resolution of every individual atomic column. This would make it possible to see if there are homoatomic bonds (In-In or P-P) across a twin interface, thus enabling the interface structure to be determined. If we instead look at InP in a $\langle 112 \rangle$ projection this

distance is only 0.08 nm, requiring a much higher resolution.

2.1 The intrument

In figure 2.1 (a) a photograph of a medium voltage (which in the context of TEM is 200-300 kV) transmission electron microscope is shown together with a schematic drawing (b). The whole column needs to be evacuated as the electrons would otherwise be scattered too much by the gas molecules. The microscope can be divided into three sections: the illumination system, the image forming system, and the projection system. The description of the basic workings of a TEM in this section follows Williams and Carter[14], unless other references are given.

The illumination system consists of the electron gun and a series of lenses with the purpose of projecting a uniform and ideally parallel (but in reality slightly convergent) beam of electrons onto the sample. The gun itself is basically a filament which is either heated until it emits electrons (thermionic gun) or subjected to a very strong electric field which extracts electrons from the tip (field emission gun, FEG). The FEG has the great advantage of emitting electrons from a very small region and with a very small spread in energy (and consequently a small spread in wavelength), making the illumination highly coherent. This is very important for high resolution imaging and even more so for image series reconstruction, as will be shown later. Often even FEGs are somewhat heated (and are then called Schottky sources, in contrast to the unheated cold-FEGs), trading a small increase in energy spread for more electrons emitted and less stringent vacuum requirements. Both microscopes used in this thesis employ a Schottky source. The potential drop in the accelerator tube, the acceleration voltage, determines the wavelength of the electrons. At 200-300 kV the electrons have a wavelength of 0.00250-0.00192 nm and travel at approximately 2/3 the speed of light. Despite this large velocity the sample needs to be very thin, at most a few hundred nanometres, in order not to scatter the electrons too much.

The illumination system also contains the condenser aperture, which allows the electrons emitted at high angles to be excluded at the cost of reducing the beam current. This allows the convergence angle of the illumination to be controlled (usually this means to minimize it for a certain diameter of illumination on the sample).

The image forming system contains the sample and the strongest lens in the microscope: the objective lens. In the discussion of high resolution imaging later this is where everything of interest takes place: the whole illumination system is described by a few simple parameters while the projection system is more or less ignored. The sample and objective lens are shown in more detail in figure 2.1 (c), where a ray-optics description of the image formation is shown. A parallel illumination interacts with the sample, is scattered and then brought to a focus by the objective lens. Note that rays scattered to

[1] Photo courtesy of Gunnel Karlsson

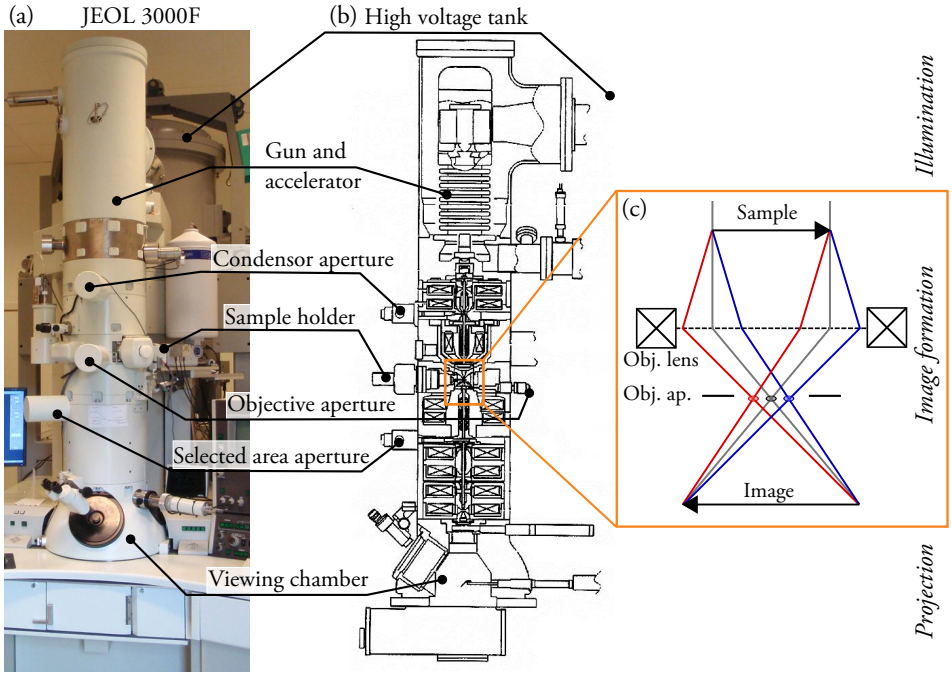

Figure 2.1: (a) Photo of the 300kV JEOL 3000F TEM in Lund[1] with a few of the principal elements marked. (b) Cross-section illustration of the same instrument. (c) Ray diagram of the image forming (objective) lens showing the location of the diffraction pattern in the back focal plane.

the same angles are focused into points in the back-focal plane, forming the diffraction pattern. Even when dealing mostly with imaging the diffraction pattern is very important: the distribution of intensity between the different spots gives a clear indication of the sample orientation, allowing the crystals to be tilted to the desired viewing direction.

Two apertures are also included in the image forming system: the objective aperture and the selected area aperture. The objective aperture is inserted into the back-focal plane and excludes electrons scattered above certain angles, which is very important for the contrast and quality of the images. The selected area aperture is located in a conjugate image plane: if inserted only electrons from a small part of the illuminated area are allowed to pass. This allows diffraction patterns to be collected from small areas even with a wide, and therefore less convergent, illumination.

The projection system is responsible for projecting and magnifying either the image or the diffraction pattern formed by the objective lens. In order to see the final image it is projected onto either a phosphorescent screen for quick viewing or onto a scintillator fiber-optically coupled to a CCD detector for recording digital images (there are other

recording devices, but only CCDs were used in this thesis). The process of converting a continuous signal to a discrete, pixelated image will reduce any rapidly varying contrast. In addition there is some scattering of the impinging electrons and the generated photons in the scintillator which also reduces the contrast. This detector related degradation of the image is described by the modulation transfer function (MTF) and can be measured by imaging a known object, such as a sharp edge.[15]

Contrast in conventional TEM

There are many different mechanisms for generating contrast in TEM. For the purpose of forming images in TEM the electrons are best described as waves, and the contrast mechanisms can therefore be divided according to whether they rely on modifying the amplitude or the phase of the transmitted waves. The description of phase contrast used in high resolution imaging will occupy much of the remainder of this chapter, but a brief description of two other important mechanisms relying on differences in amplitude is in place. Mass-thickness contrast relies on the fact that heavier elements or thicker areas of the sample scatter more of the incoming electrons to high angles. These high angle electrons are then excluded from the image by the objective aperture or by the column itself, making these areas in the image dimmer. Diffraction contrast works by a very similar mechanisms but relates more specifically to when a smaller objective aperture is used to select only a single or a few diffraction spots. In that case only areas which diffract in this very specific direction will have any intensity in the image.

2.2 High resolution imaging

Figure 2.2 shows the image forming system from a wave-optics perspective. The electrons passing close to the atoms in the sample will be slightly accelerated by the electrostatic potential compared to the electrons passing through the voids, shifting their relative phases. This is described by the *phase object approximation* where the phase shift depends on the projected potential of the sample along the path of the electron, V_t, and an interaction parameter, σ. If the phase shift is small this can be simplified to a linear expression in the *weak phase object approximation*, as in equation 2.1. The physical meaning of this is that some of the electrons passing by the atoms are scattered with a $\pi/2$ phase change.

$$\psi_o = \exp\left[-i\sigma V_t(x)\right] \approx 1 - i\sigma V_t(\mathbf{x}) \tag{2.1}$$

The information about the sample is in other words contained in the phase of the object wavefunction (which is used interchangeably with exit wavefunction), ψ_o. However the detector can only register amplitude and so a pure phase object imaged by a

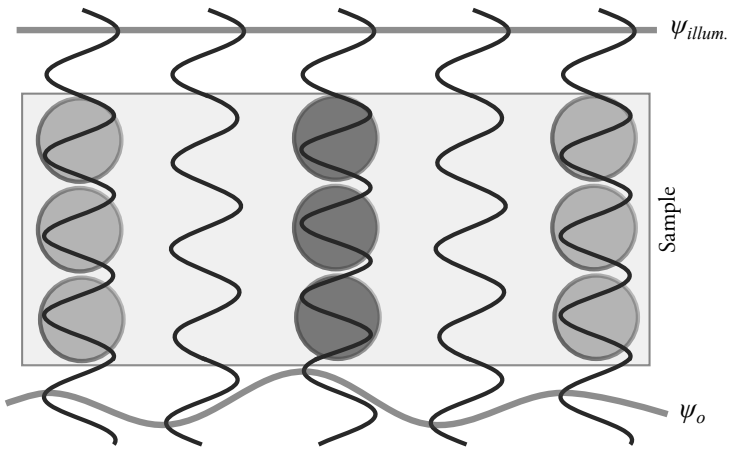

Figure 2.2: Electron wave interaction with a weak phase object, in this case a sample a few atoms thick. The potential of the atoms cause a phase lag between the wave at the atomic positions and at the empty spaces. Atoms and wavelengths are not to scale.

perfect lens would not produce any contrast. We get contrast in phase images due to the aberrations in the objective lens which add a further phase change to the scattered electrons, resulting in an image wavefunction $\psi_i \neq \psi_o$. Ideally the total phase change of the scattered electrons should be π, causing destructive interference with the unscattered electrons, which results in high potential areas in the sample being dark in the image.

The weak phase object approximation is only strictly correct for very thin samples: even a single heavy atom could break the condition that the phase shift should be very small. An even bigger problem is that the projected potential model is invalid for thicker samples where multiple scattering is significant, which makes a 2D potential distribution an inadequate description.

The phase contrast transfer function

For a more detailed description of how the lens aberrations affect the images we start by looking closer at the image contrast. In the following, lower case functions are in real-space with $\mathbf{x}$ denoting the coordinate and upper case functions are the equivalent in reciprocal space where $\mathbf{k}$ denotes the coordinate. These are related by Fourier transformation as shown for the image contrast, c, below:

$$c(\mathbf{x}) = \psi_i \psi_i^* \Rightarrow C(\mathbf{k}) = \mathcal{F}c(\mathbf{x}) = \Psi_i \star \Psi_i^* \tag{2.2}$$

The convolution of the image wavefunction with its conjugate can be simplified in the case of a weak phase object where most of the intensity remains in the unscattered beam. In that case it is sufficient to consider only the interference between the unscattered beam and the scattered beams, ignoring any contribution from interference between two or more of the scattered beams. This reduces the convolution integral to a sum and is therefore called the *linear imaging approximation*. Ψ_i can now be expressed as the object wavefunction, Ψ_o, multiplied by a transmission coefficient, T, which describes the phase change caused by the objective lens relative to the unscattered beam. T can in turn be expressed in terms of how many wavelengths difference there is between the two beams depending on the reciprocal coordinate of the scattered beam, $\chi(\mathbf{k})$.

$$\begin{aligned} C(\mathbf{k}) &= \Psi_o(\mathbf{k})T(\mathbf{k}) + \Psi_o^*(-\mathbf{k})T^*(-\mathbf{k}) \\ &= \Psi_o(\mathbf{k})\exp\left[i\chi(\mathbf{k})\right] + \Psi_o^*(-\mathbf{k})\exp\left[-i\chi(-\mathbf{k})\right] \end{aligned} \tag{2.3}$$

By noting that the object wavefunction as described by the weak phase object approximation in equation 2.1 is conjugate anti-symmetric, $\Psi_o(\mathbf{k}) = -\Psi_o^*(-\mathbf{k})$, this becomes:

$$\begin{aligned} C(\mathbf{k}) &= \Psi_o\left(\exp i\chi(\mathbf{k}) - \exp -i\chi(-\mathbf{k})\right) \\ &= \Psi_o\left[\cos\chi(\mathbf{k}) + i\sin\chi(\mathbf{k}) - \cos\chi(-\mathbf{k}) + i\sin\chi(-\mathbf{k})\right] \end{aligned} \tag{2.4}$$

The aberrations causing χ are either even functions, $\chi(\mathbf{k}) = \chi(-\mathbf{k})$, or odd functions, $\chi(\mathbf{k}) = -\chi(-\mathbf{k})$. In either case the cos terms disappear. Substituting the weak object approximation for Ψ_o we are now left with:

$$C(\mathbf{k}) = \Psi_o 2i\sin\chi(\mathbf{k}) = \delta + 2\sigma V_t(\mathbf{k})\sin\chi(\mathbf{k}) \tag{2.5}$$

The $\sin\chi$ term is called the phase contrast transfer function (pCTF) and describes how phase information in the object wave function is transferred to image contrast for a *weak phase object* and *linear imaging* conditions. Equation 2.5 makes the goal of HRTEM clear: set the aberrations so that $\chi = -\pi/2$ (or $\pi/2$ if you are operating an aberration corrected microscope). This makes the $\sin\chi$ term equal to -1 allowing you to directly image V_t, which is related to the atomic positions in your sample.[16, 17]

Aberrations

The origin of the phase change function χ is illustrated in figure 2.3, where the spherical wavefront emitted from a point in the object is brought to focus by the objective lens. Ideally it should be focused to a single point in the image, but the wavefront is displaced

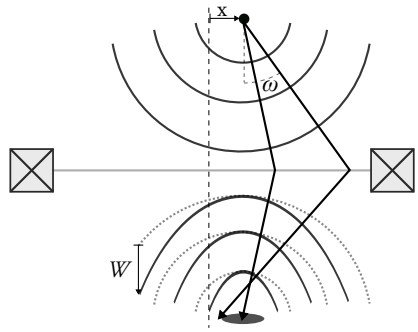

Figure 2.3: A wave optics description of a point being imaged by an imperfect lens to a disc. The distance between the ideal, spherical, wave and the actual wave is given by W, which is a function of both position, $\mathbf{x}$, and angle, ω, to the lens.

Table 2.1: The wave aberration function with terms up to fourth order in $\mathbf{k}$.

$W(\lambda\mathbf{k}) = \Re\{$	$A_0\lambda\mathbf{k}^*$	Image shift
	$+\frac{1}{2}A_1\lambda^2\mathbf{k}^{*2}$	Twofold astigmatism
	$+\frac{1}{2}C_1\lambda^2\mathbf{k}^*\mathbf{k}$	Defocus
	$+\frac{1}{3}A_2\lambda^3\mathbf{k}^{*3}$	Threefold astigmatism
	$+\frac{1}{3}B_2\lambda^3\mathbf{k}^{*2}\mathbf{k}$	Axial coma
	$+\frac{1}{4}A_3\lambda^4\mathbf{k}^{*4}$	Fourfold astigmatism
	$+\frac{1}{4}S_3\lambda^4\mathbf{k}^{*3}\mathbf{k}$	Axial star
	$+\frac{1}{4}C_3\lambda^4\mathbf{k}^{*2}\mathbf{k}^2\}$	Spherical aberration

a certain distance by the lens aberrations. This distance, W, called the wave aberration function is generally a function both of the position, $\mathbf{x}$, of the point on the sample and the scattering angle, ω. Since only small areas are imaged at a time in HRTEM the dependence on $\mathbf{x}$ is usually ignored (the *isoplanatic approximation*). The scattering angle can be converted to a reciprocal coordinate using the electron wavelength, λ, according to $\omega = \lambda\mathbf{k}$. In table 2.1 the wave aberration function is shown with all terms up to fourth order in $\mathbf{k}$.[16, 18]

For microscopes without an aberration corrector we can usually ignore all aberrations except defocus, C_1, twofold astigmatism, A_1, and spherical aberration, C_3. Twofold astigmatism causes a smearing of the image in one direction, but can be compensated by stigmator coils which provide a counteracting effect. Spherical aberration

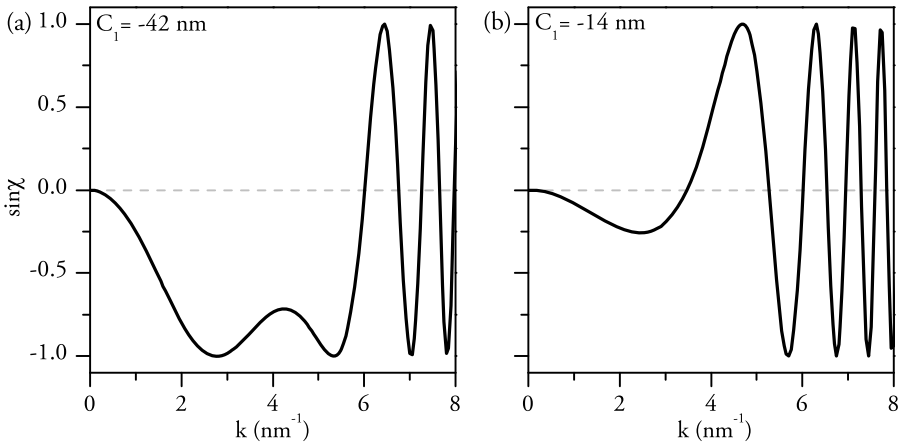

Figure 2.4: Phase contrast transfer function for: (a) optimum defocus which shows a large pass-band of equal transfer up to about 6 nm^{-1} (which defines the maximum resolution of 0.17 nm), and (b) minimum contrast defocus. Parameters were chosen to match a JEOL 3000F (300 kV, $C_3 = 0.6$ mm).

on the other hand is unavoidable in round magnetic lenses and causes high angle rays to be focused closer to the lens than lower angle rays.[19] This is by far the largest contributor to the aberration function in an uncorrected microscope and is the aberration used for the illustration in figure 2.3. Keeping only defocus and spherical aberration we can now convert the wave aberration function to a phase change, and since both C_1 and C_3 are rotationally symmetric we can substitute the scalar spatial frequency k for the complex reciprocal vector $\mathbf{k}$:

$$\chi(k) = \frac{2\pi}{\lambda} W(k) = 2\pi \left[\frac{1}{4}\lambda^3 C_3 k^4 + \frac{1}{2}\lambda C_1 k^2 \right] \tag{2.6}$$

By setting the defocus to a negative value it is possible to offset the effects from the large positive spherical aberration and get the correct phase shift for a large set of k. Figure 2.4 shows $\sin\chi$ for a 300 kV microscope with $C_3 = 0.6$ mm (JEOL 3000F) for two different defoci. At $C_1 = -42$ nm there is a large spatial frequency range from 0 to 6 nm^{-1} where all phase information in the object wavefunction is transmitted correctly to the image. This condition defines the optimum defocus, $C_{1,opt}$, and the optimum resolution R_{max}:

$$C_{1,opt} = 1.2\sqrt{C_3\lambda} \approx 42 \text{ nm} \tag{2.7}$$

$$R_{max} = 1/k_{max} = 0.64\,(C_3\lambda)^{\frac{1}{4}} \approx 0.17 \text{ nm} \tag{2.8}$$

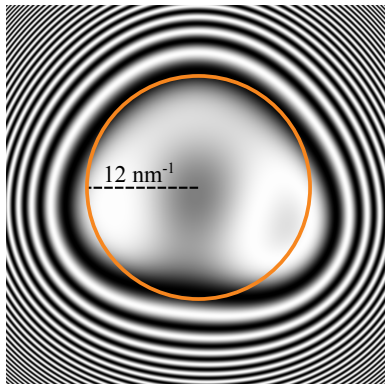

Figure 2.5: $\sin\chi$ after tuning the aberration corrector on the 200 kV JEOL 2200MCO.

After the phase contrast function crosses the k axis the first time the spherical aberration will again dominate and as a result the function oscillates. This results in an out of phase transfer of the higher spatial frequencies (that is the smaller distances in real space) making the image difficult to interpret. In normal HRTEM this problem is reduced by inserting an objective aperture which hinders all spatial frequencies above some k from contributing to the image, ideally allowing only the correctly transferred frequencies through. At $C_1 = -14$ nm the transfer of short spacial frequencies is mimimized. This is the minimum contrast condition which is used experimentally as a visual clue to the defocus.

The assumption that only defocus and spherical aberration will contribute to χ is not correct at resolutions approaching 0.1 nm. Here even the smaller aberrations will have significant effects and the aberration function is no longer rotationally symmetric. The full $\sin\chi$ for an aberration corrected microscope at optimum defocus is illustrated as a 2D image in figure 2.5 together with the resolution limit imposed by the sum of all aberrations.

Effects of limited coherence

In a real microscope the illumination is not perfectly parallel and monochromatic. Small fluctuations in acceleration voltage, lens currents and the energy spread of the gun results in some variations of the illumination wavelength. Since the objective lens has a strong chromatic aberration the low energy electron are focused more strongly, resulting in a defocus spread of a few nanometres instead of a single defocus value.

In order to form a parallel illumination a point source would be needed. Since all electron sources have a finite size there is a always some distribution of different illumination directions.

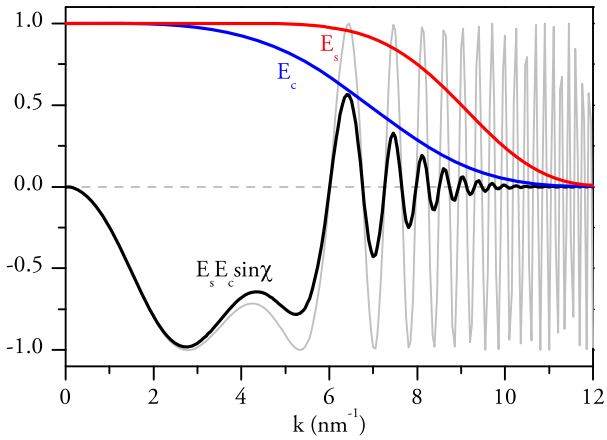

Figure 2.6: Phase contrast transfer function at optimum defocus as in figure 2.4, but with damping functions corresponding to the limited coherence caused by having a finite source size (0.2 mrad convergence semi-angle) and a distribution of slightly different wavelengths (giving 4 nm defocus spread).

When an image is recorded there is an incoherent summation of many intensities, each one formed under slightly different conditions as explained above. A change in illumination direction results in a shift of the aberration function to a new origin. The effect of a defocus spread, ΔC_1, can be seen directly from equation 2.6. In both cases the rapidly varying parts of the phase contrast transfer function will be averaged away, resulting in a loss of transfer at high spatial frequencies. Under the linear imaging approximation these effects can be described by envelope functions which are multiplied to the $\sin\chi$ term in equation 2.5, with E_c being related to defocus spread, and E_s being related to illumination convergence (with convergence semi-angle α):

$$C(k) = \delta + 2\sigma V_t(k) E_c E_s \sin\chi(k) \tag{2.9}$$

$$E_c(k) = \exp\left[-\frac{1}{2}(\pi\Delta C_1)^2 k^4\right] \quad \left(\text{from: } \frac{\partial\chi}{\partial C_1}\right) \tag{2.10}$$

$$E_s(k) = \exp\left[-\left(\frac{\pi\alpha}{\lambda}\right)^2 \left(C_3\lambda^3 k^3 + \lambda C_1\right)^2\right] \quad \left(\text{from: } \frac{\partial\chi}{\partial k}\right) \tag{2.11}$$

The effect of these envelope functions are shown in figure 2.6 for reasonable values for the JEOL 3000F. It can be seen that the chromatic aberration provides the ultimate limit to resolution in the absence of other aberrations. The limit where the chromatic aberration reduces the phase contrast to zero is called the information limit of the microscope.[14] It should be noted that variations in the specimen during the image

acquisition will also result in the incoherent of the different configurations. Because of this, additional envelope functions for specimen vibration and drift can be added.[20]

2.3 Correction of lens aberrations

Two methods of aberration correction are used in paper I: hardware correction and focal series reconstruction. With hardware correction additional, non-round lenses allows the tuning of all aberrations up third order, making it possible to achieve phase contrast without reversals up to the information limit of the microscope.[21] Focal series reconstruction instead aims to recover first the complex image wave function containing both phase and amplitude information, and then correct the phase and amplitude changes to get the object wavefunction. This is fundamentally different from hardware aberration correction which still results in normal phase contrast images, albeit with much smaller (but not zero) aberrations than conventional HRTEM. The drawback is that it is an off-line method, requiring processing of several images recorded with different defocus in order to arrive at an aberration free object wavefunction.

These two methods benefit from being used together. Hardware aberration correction typically measures and minimizes high order aberrations not accessible to focal series reconstruction. The low aberrations also minimizes delocalization and the spatial coherency envelope function. Focal series reconstruction on the other hand remove the remaining aberrations at the site of interest and corrects for amplitude variations in the phase contrast transfer function.[16, 22]

There are more methods available for aberration correction than mentioned above. Electron holography can also be used to get the image wave function, which can be corrected just as for focal series reconstruction.[19] Tilt series reconstruction is very similar to focal series reconstruction, but uses varying illumination tilt instead of defocus. Since tilting the illumination shifts the temporal coherency envelope it is possible to get beyond the information limit using this method, but it requires a very thin sample and is more difficult to carry out.[16] Independent which method is used the first step is to measure the aberrations accurately.

Measuring the aberrations

The symmetric aberrations can be measured directly from images of an amorphous object, such as the carbon support film on the grids, as they have a wide and continuous distribution of spatial frequencies. Equation 2.5 suggests that the phase contrast transfer function will be directly visible in this case as any zero crossing will remove that particular spatial frequency from the image. Fourier transforms of images (called diffractograms) of amorphous objects will therefore contain dark rings whose spacings are related to defocus and spherical aberration, while any deviation from a circular shape

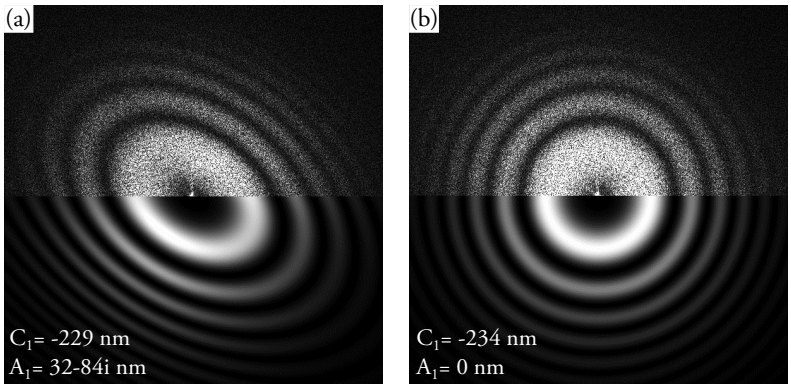

Figure 2.7: Experimental diffractogram of amorphous carbon (top) matched with simulated phase contrast transfer functions for a 300 kV TEM with $C_3 = 0.6$ mm. (a) With twofold astigmatism, and (b) with only defocus.

is related to twofold astigmatism. In this way the diffractograms can be directly matched to the phase contrast transfer function. Such a matching is illustrated in figure 2.7.

For very high resolution it is important to also measure the antisymmetric aberrations. By tilting the beam the origin of the wave aberration function is shifted and high order aberrations will induce additional defocus and twofold astigmatism. By measuring these for a series of different beam tilts all aberrations present under axial illumination can be determined. Such a tableau of diffractograms of an amorphous object recorded with varying beam tilts is called a Zemlin tableau.[23] This method is implemented in the alignment routine of the CEOS imaging aberration corrector on the JEOL 2200MCO.[24]

The downside of this method is that there can be no crystalline material in the images used for the measurements as they have discrete diffractograms with high amplitude spots. These would dominate over the continuous amorphous signal used for measuring the phase contrast transfer function. For this reason it is necessary to measure the aberrations on an area separate from the area of interest where the images are recorded. To avoid this problem it is possible to use only the diffractogram phase and compare it with calculated phases for different phase contrast transfer functions. This has the advantage that the crystalline reflections are suppressed, making it possible to measure the phase contrast transfer function even from almost purely crystalline areas (i.e. your area of interest on the sample). Matching with calculated phase patterns does however take more time than measuring the aberrations directly and is used only for post processing of images.[25]

Hardware correction

For round magnetic lenses there is always a positive spherical aberration, which will be the single largest contribution to the wave aberration function. With hardware aberration correctors extra multipole lenses, which do not have this constraint, are added to the microscope. In this way the total spherical aberration of the objective lens and aberration corrector can be tuned by making the two add up to either a small positive or negative value.[26] The effect of a single multipole lens is however not spherically symmetric and as a result a single such lens could only correct the spherical aberration for some azimuths and would introduce additional aberrations. For these reasons aberration correctors contain many lens elements (likely more than the rest of the TEM taken together), making computer assisted alignment necessary.

For the purpose of image formation the same equations apply as for uncorrected microscopes, only using lower coefficients for the aberrations. The largest difference is that with an aberration corrector the spherical aberration, in addition to the defocus, is accessible to the user and equation 2.7 can no longer be used to unambiguously define the optimum condition. There are many suggestions in the literature as to how the optimum conditions for C_3 and C_1 should be defined: compensating for the uncorrected fifth order spherical abberation (C_5),[27] setting the first crossover of the optimum resolution to the information limit,[27] or minimizing the contrast delocalization up to the desired resolution.[28] The differences between these proposed optimum conditions are however mainly in the sub 0.1 nm resolution range.

A more important distinction for the resolutions used in this thesis is between positive and negative spherical aberration (together with a negative or positive defocus respectively). For the latter case the phase contrast transfer function results in bright atomic positions (total phase shift of 0), instead of dark atomic positions (total phase shift of π at the atom positions). This becomes important when considering samples where the weak phase object approximation is not valid, that is for almost all samples of realistic thicknesses. The image will then contain non-linear interferences between the scattered beams in addition to the linear term. For normal, positive C_3 the non-linear contrast will detract from the linear contrast (which provide the structure information), while in the negative C_3 case they will add.[29] This is particularly advantageous when imaging light atom columns in the vicinity of heavy atom columns, such as oxygen in metal oxides.[30, 31] It is however still important to simulate images for the particular conditions in your sample, as there is no guarantee even with negative C_3 that the structure will be represented in an interpretable way in the images.

Software correction: image series reconstruction

The aim of image series reconstruction is to find the complex object wavefunction, given a set of images and their aberrations. As suggested by equation 2.2 the relation-

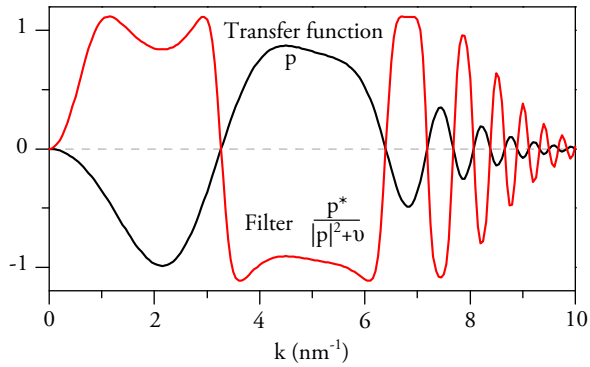

Figure 2.8: Phase contrast transfer function and corresponding Wiener filter for a single image with transfer function p. When applied the filter will correct the phase (due to p^*) and amplitude (due to $1/\left|p\right|^2$) of the transfer function, without amplifying noise from the regions with little or no information transfer (due to the noise reduction term ν).

ship between image and object wavefunction is quite complicated in the full treatment of image formation, making iterative methods necessary. In the linear imaging approximation on the other hand the object wavefunction can be directly approximated from the images. Comparisons between the two classes of methods show that the phase of the object wavefunction can be retrieved by the linear method as long as the non-linear contributions to the image are small, but that the amplitude in addition requires that most intensity remains in the direct beam. For Si [110] this gives a limit of 14 nm for phase but only 4 nm for amplitude.[32] Simulations of 10 nm GaAs indicate that major improvement in the reconstruction from using a full non-linear method is for the amplitude.[33]

The linear imaging solutions can be derived in many different, but equivalent, ways.[34] The reconstructions in this thesis have been performed using a Wiener-filter based method together with a series of images recorded at different defocus.[25] This approach could also be used with images recorded at different illumination tilts.[35] In this case the object wavefunction is estimated as in equation 2.12, where r_i is a filter function, which is based on both the aberrations in image i and in all other images in the series, and C_i is the image. Figure 2.8 illustrates this approach for a single image.

$$\Psi'_o = \sum_i r_i C_i \tag{2.12}$$

It is difficult to see the workings of the filter function r_i from its full expression (see reference [25]). A qualitative description is as follows: for a Fourier component

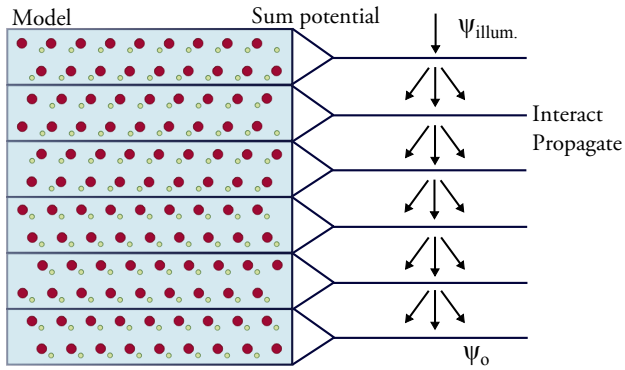

Figure 2.9: Principle steps in TEM image simulation by the multislice method. A model structure is cut into thin slices perpendicular to the electron wave, each one thin enough for the weak phase object approximation to hold. The electron wave then has alternating interaction with each slice, followed by free space propagation to the next.

that is transfered in some of the images in the series the filter simply averages them and corrects any phase change, if instead the Fourier component is not transfered in any of the images (or only transfered very weakly) the filter tends to 0 in order to reduce the noise. For a single image this function becomes much simpler, as can be seen from figure 2.8 where the filter function contains only the transfer function p and a noise term v. As the transfer inevitably is damped at high spatial frequencies by the defocus spread, this sets the ultimate limit for focal series reconstruction.

Applications of image series reconstruction for III-V materials includes imaging of dislocations in GaAs[36] (also in combination with hardware aberration[37]), and compositional mapping of heterojunctions in AlGaAs-GaAs and InAs-InGaSb.[38]

2.4 TEM image simulation

The image formation theory as outlined earlier also serves as the basis for simulating TEM images. The simulations in this thesis were performed using the multi-slice approach, which is briefly outlined. From a model of the atomic positions the projected potential is calculated and applied to the electron wave as in the weak phase object approximation. To allow for thicker samples the model is sliced into several slabs orthogonal to the incident beam, with each individual slab being thin enough to be described as a weak phase object (in the order of 0.2 nm). Between each interaction of the electron wave with the projected potential of a slab the wave is subject to free space propagation. In this way the object wave function is generated after the electron wave has interacted with each slice of the model.[39] The concept behind multi-slice simulations is illus-

trated in figure 2.9.

Simulated and experimental images can be compared in terms of intensity, contrast and pattern. While patterns can be readily matched, contrast is usually much larger in simulated images by as much as a factor of three.[40] There is no one good candidate for this discrepancy, but possible candidates include: scattering in the camera and scintillator,[41] many small errors from e.g. amorphous layers and inelastic scattering together with errors in the modelling of the imaging system,[42] or thermal diffuse scattering.[43] For this thesis only visual comparisons of patterns were used.

2.5 Scanning transmission electron microscopy

The basic principle of scanning transmission electron microscopy (STEM) is illustrated in figure 2.10 (a). Instead of forming a broad parallel beam on the sample as in conventional TEM the illumination system forms a small and convergent probe. This probe is then scanned across the specimen in a grid with the signal at each pixel formed from the number of electrons falling on the various STEM detectors; either brightfield collecting the direct disc (BF) or annular dark field (ADF) collecting diffracted or high angle scattered electrons.[14]

STEM brightfield images can be considered completely analogous to conventional TEM images, but there are two areas where STEM has advantages. The first concerns high angle annular dark field (HAADF) images, which are formed from an incoherent summation of electrons scattered to very high angles and has no direct equivalent in conventional TEM. This imaging mode (with advantages such as a linear signal over larger sample thicknesses, contrast related to atomic number and no phase inversions with defocus[14]) has not been used extensively for the work in this thesis. The second advantage with STEM is that spectroscopy can be performed at each position of the probe enabling spatially resolved micro-analysis. Spectrum imaging, where a full spectra is recorded at each pixel in the image, in particular shows the benefit of combining STEM and spectroscopy.[44]

2.6 Energy dispersive X-ray spectroscopy

The imaging techniques described so far rely on elastically scattered electrons, but there are of course also inelastic processes occurring as the beam passes through the sample. Figure 2.10 (b) shows an incoming fast electron transferring enough energy to kick out one of the inner-shell electrons of an atom in the sample, which is left in an excited state. At this point one of the electrons from an outer shell can transfer to the vacant position in the inner shell, and in the process a photon is emitted. The energy of this photon is characteristic of the atom (and which shells were involved) and can be used to identify (depending on the energy of the photon) and quantify (depending on the

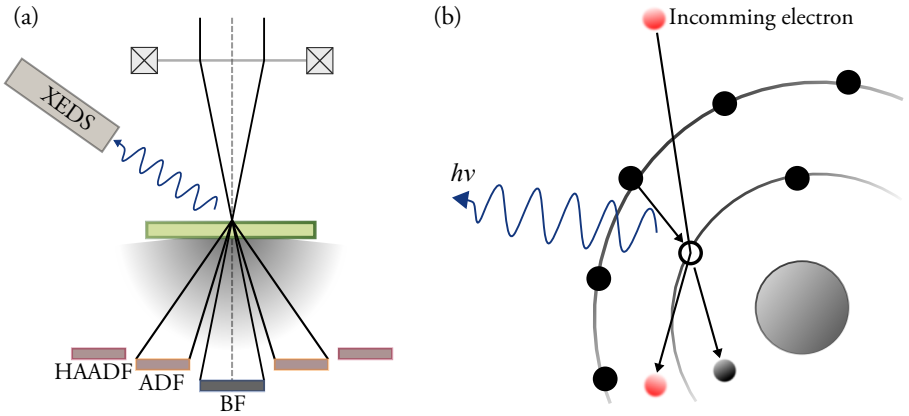

Figure 2.10: (a) Principle behind scanning transmission electron microscopy (STEM), where the electron beam is focused to a small probe which is scanned across the sample. The image is constructed serially with either electrons scattered to different angles, or from X-rays. (b) Formation of characteristic X-rays from an atom hit by a fast electron from the STEM probe.

number of photons) the elements in the sample by means of an energy dispersive X-ray spectrometer.[14]

The spatial resolution is limited by the size of the electron beam as it passes through the sample, which in turn depends on the size of the incident beam and how much it is broadened by scattering in the sample. Assuming single scattering this can be estimated to be on the order of 2 nm at best in 50 nm thick InP.[45]

The minimum detectable fractions of an element by XEDS is somewhere around 0.5-1 atomic%. This might seem not very sensitive, but only a small volume of atoms are analysed so this can correspond to detecting only a handful of atoms. The detection limit of course depends on the current in the probe and collection time, as the signal to noise ratio will increase with an increasing number of counts. This comes at the expense of having a larger probe and damaging the sample more. Also the thickness of the sample matters: for a sufficiently thin sample the small volume which the probe passes through might not contain any of the trace elements.[14]

Chapter 3

Nanowires

3.1 Growth

Nanowire growth is an example of epitaxy, meaning that the substrate crystal structure strongly influences the structure of the grown crystal (in this case the nanowire). For III-V materials grown on a substrate made of the same material (homoepitaxy), another III-V material or a group IV material like Si (heteroepitaxy) the grown material will continue with the same crystal structure and direction as the substrate, since the atoms in all these materials are stacked in the same fashion (albeit with different spacing, i.e. different lattice parameters). Ideally this will make the substrate and nanowire, including any heterostructure, a single crystal.

Material for the epitaxially growing crystal can be supplied in many different ways: in a liquid phase, in the gas phase as a vapour of the pure elements or as chemical compounds (precursors) which will decompose at the substrate to yield the desired material. These methods can be further divided according to their operating pressure and the chemistry of the precursor gases. The nanowires used in this thesis were all grown using Metal Organic Vapour Phase Epitaxy (MOVPE) operated at moderate pressures (100 mbar) utilizing metal organic precursors for the group III elements and hydrides for the group V. In this way InP is synthesized from trimethyl indium (TMIn) and phosphine (PH_3) resulting in the following total reaction:

$$\mathrm{In(CH_3)_3(g) + PH_3(g) \longrightarrow InP(s) + 3\,CH_4(g)}$$

In reality this occurs in many steps in a complicated process and there is always a risk in MOVPE that carbon is incorporated due to incomplete elimination of the organic ligands.[46]

Compared with normal epitaxy nanowire growth involves one more complication: how to ensure that the growth only occurs at specific sites on the substrate in the form of nanowires and not evenly over the entire surface. To accomplish this one can either use a

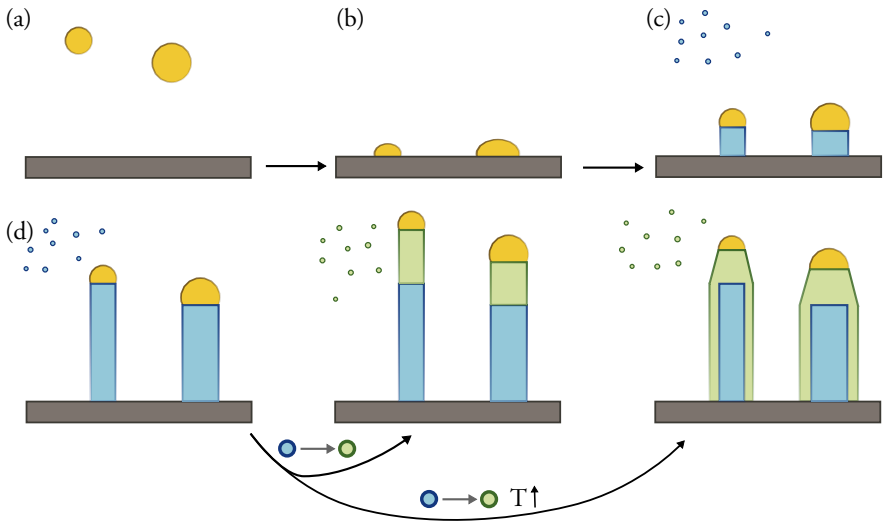

Figure 3.1: Principle behind gold assisted metal organic vapour phase epitaxy (MOVPE) of nanowires. By changing the precursors it is (under some conditions) possible to form axial or radial heterostructures.

mask to limit growth to small openings[47] or place nanometre sized metal particles on the surface with the effect that nucleation of new material only occurs underneath these particles. In this way the position and diameter of the nanowires can be controlled by the position and diameter of the nanoparticles respectively. For nanoparticle catalysed MOVPE nanowire growth of III-V materials gold is the most common choice and this was used for all nanowires analysed in this thesis. Messing et al. give a detailed description of the many different methods available to generate such gold nanoparticles.[48]

Figure 3.1 illustrates the nanowire growth process using gold seeded MOVPE. A more specific description using homoepitaxy of InP as an example is given in parenthesis after each step (from paper I). (a) Gold particles are deposited on the substrate surface (InP with an atomically smooth surface). (b) The substrate is heated under a flow of group V using H_2 as a carrier gas in order to desorb any surface impurities or oxides (550 °C, 6 L/min H_2 with a molar fraction of PH_3 on the order of 1×10^{-2}). (c) The temperature is lowered to a point where little or no material will nucleate, except underneath the gold particles, and the group III precursor is added to the flow (420 °C, TMIn molar fraction on the order of 1×10^{-5}). The precursors decompose and the elements alloy with the gold particle, either by impinging on it directly or after diffusing on the surface. At some point the concentration of these elements in the gold particle reaches a critical level and a nucleus of solid III-V material is formed at the three-phase boundary between the liquid (or solid) gold particle, the gaseous surroundings and the

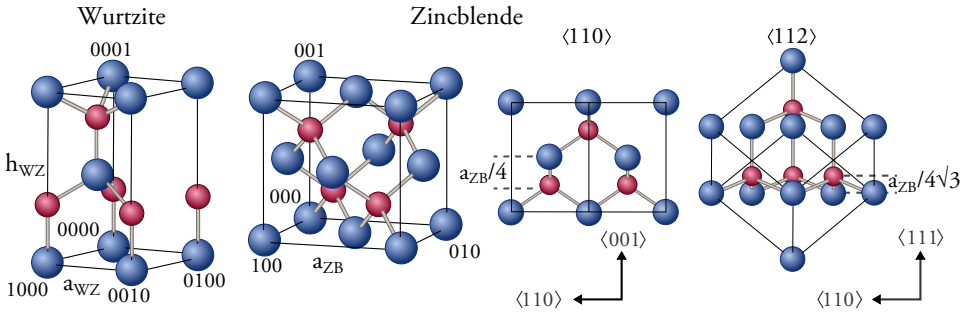

Figure 3.2: Unit cell of the hexagonal wurtzite and the cubic zincblende structure, which III-Vs adopt. Also shown is the ⟨110⟩ and ⟨112⟩ projections of the zincblende structure, with the smallest "dumbbell" spacing between the III and V atoms marked.

solid substrate or nanowire. When a stable nucleus has formed more growth species quickly attach and expands it until a whole new layer of III-V material has been formed underneath the gold particle. (d) The group III precursor is kept on until the nanowires have reached the desired length. During this period the group III or group V precursors can be changed in order to create a heterostructure, or the temperature can be increased to enable nucleation on the nanowire sides in order to form a shell around the nanowire. When the desired structure has formed, the group III precursor flow is turned off and temperature lowered to room temperature in order to stop the growth.

3.2 Crystal structure

In nanowires III-V materials show polytypism and can adopt one of two crystal structures: the hexagonal wurtzite or the cubic zincblende structure. In bulk zincblende is the most common structure (with only nitrides being wurtzite) and can be described as two interpenetrating face centered cubic lattices with the origin of the group III lattice at (0,0,0) and the group V at (1/4,1/4,1/4). This means that it is not centro-symmetric; for instance the $\{111\}$ planes are group III terminated while the $\{\bar{1}\bar{1}\bar{1}\}$ planes are terminated by group V atoms. In the notation used for III-V materials this is often emphasized by appending A to denote directions or planes terminated by group III atoms, and conversely B for group V terminated planes and directions. The zincblende and wurtzite structures are illustrated in figure 3.2. In the ⟨112⟩ projection the atoms line up in such a way as to make the polytypes indistinguishable from each other. The projected distances between the atoms are also smaller in this case than when the structure is rotated 30° and viewed in the ⟨110⟩ direction. For these reasons the ⟨112⟩ viewing direction is not used in any of the following illustrations, nor is it used in practice at the TEM in any of the papers in this thesis.

Nanowire growth is usually carried out on (111)B substrates and the nanowires grow in a ⟨111⟩B direction. The growth then proceeds by adding one (111) bilayer at a time and the final structure evolves through the stacking of many such layers. This is illustrated in figure 3.3 (a) and (b) which shows how there are two possibilities of adding a new layer: either the new layer has the same bond directions as the preceding one or it is rotated by 60°. In the former every third layer is identical, while in the latter every other is identical. If we letter each bilayer according to its position we have either a hexagonal . . . ab. . . stacking or a cubic . . . abc. . . stacking, which have the wurtzite and zincblende structure respectively. In reality it is a bit more complicated than this as the change in stacking sequence also slightly changes the bond distances.[49] It is possible to have stackings with more layers in the repeating sequence, for instance . . . abac. . . can sometimes be found. These additional polytypes can be systematically named according to the number of layers in the repeating sequence and the crystal system for the unit cell. The . . . abac. . . stacking is then called 4H (with H for hexagonal), while zincblende is 3C (C for cubic) and wurtzite 2H. The higher order polytypes are beyond the scope of this thesis and zincblende and wurtzite will be discussed exclusively.[50] Note that for a microscopist a bilayer is best defined to include the shortest III-V spacing since these columns will usually be imaged as a single spot in TEM. When talking about stacking sequences on the other hand a bilayer is defined to have bonds perpendicular to the layer, which simplifies the description of stacking faults and twinning.

Stacking faults and twinning

So far the focus has been on perfect crystals with a pattern of stacked layers that is repeated indefinitely. This is rarely the case for real nanowires and this is the real reason for using TEM as its strength lies in determining the local structure for very small areas (if we had a single crystal we would be better off using X-ray diffraction). Consider for instance the . . . abcbabc. . . stacking sequence where a single layer is inserted in an otherwise perfectly repeating pattern with cubic stacking. This is known as a stacking fault and is illustrated in figure 3.3 (c). There is also the possibility of changing the cubic stacking order as in the . . . abcbca. . . sequence. Now there is no single layer that has been inserted or removed, but rather there are two different zincblende structures which are each other's mirror image. These are known as twins and the plane where the stacking sequence is mirrored is called the twin plane. As shown in figure 3.3 (d-f) there is actually three different ways of forming the twin which all have different structures in the interface between the two twin segments. The first one involves a rotation of the second segment of 60° which maintain the III-V bonds also across the interface (here the crystal structure is not actually mirrored, but the stacking sequence is), and is therefore called an ortho or rotation twin. The two remaining possible interface structures form due to a true mirroring of the crystal structure, either by connecting two (111)A planes or two (111)B planes forming III-III or V-V bonds across the interface respectively.

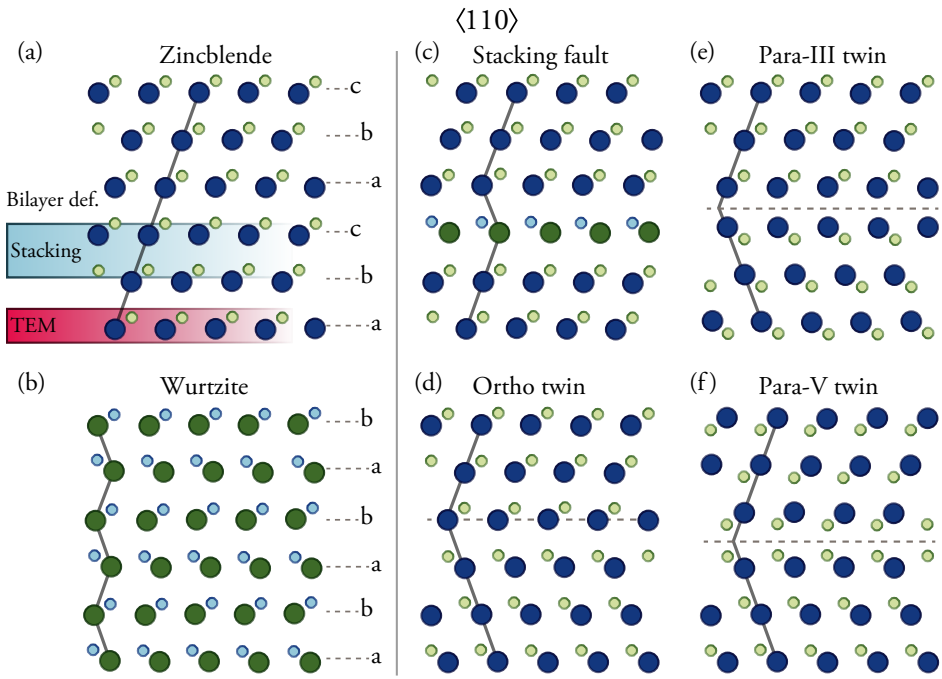

Figure 3.3: Stacking of (111) bilayers to form (a) the zincblende and (b) the wurtzite structure, viewed in ⟨110⟩. Note that there are two different perspectives as to what constitutes the bilayer. For zincblende a stacking fault (c) and three types of twins (d-f) are also shown. The twin structures differ by having either hetero- or homoatomic bonds across the interface. The faint lines underneath the structures emphasize the stacking order.

This is known as a mirror or para twin (more specifically they can be named para-III or para-V depending which type is formed).[51, 52] Note that unless the individual group III and group V columns can be resolved, these three forms are indistinguishable in the TEM.

Polytypism in nanowires

For most III-V materials (excluding nitrides) there is an extra energy on the order of 20 meV per III-V pair associated with the formation of the wurtzite crystal structure.[53] The first attempts at explaining polytypism in nanowires considered how this extra cohesive energy could be offset by wurtzite forming more favourable surfaces[54] or edges[55] for the nanowire sides. For small enough diameters these surface and edge effects will dominate allowing wurtzite to form. However this model predict wurtzite

in only the very thinnest nanowires, but this is contradicted by the fact that polytypism has been observed even in 100 nm wide nanowires.[56] Better models for particle seeded nanowire growth deal directly with the difference of creating a nucleus with either cubic or hexagonal stacking underneath the particle. Twinning can be explained in these model by having a small energy barrier to forming a wurtzite nucleus which can be overcome by higher temperatures or supersaturation, leading to a statistical distribution of twins.[57] If surface energies are also taken into account the formation of wurtzite can also be explained as the wurtzite nucleus can have lower surface energy than both the alternative zincblende nucleus and the portion of the liquid-vapour interface it replaces.[58] The last part is particularly interesting as it implies that the crystal structure of the nanowire can be controlled by affecting the liquid-vapour surface energy, by the introduction of surfactants as an example.

In nanowires we are often dealing with structures that are a mix of wurtzite and zincblende containing many twins and stacking faults. For many III-V materials it can take considerable effort to achieve a pure structure,[59] although in a few cases either zincblende or wurzite is so favored that this is not a problem. With the very mixed structures it can be very difficult to give a good description of the zincblende and wurtzite content. Should, for instance, a stacking fault or a twin be considered to contain a hexagonal segment? In terms of growth both the stacking fault and the twin definitively have layers with hexagonal stacking. On the other hand they do not appear to form barriers for the purpose of electrical properties, unlike longer wurtzite segments.[10] I think it could be argued that there is no single answer to this question and that the criteria used to classify the structure should be adapted to the context in which this data is to be used.

3.3 Additional steps during growth: doping and etching

In order to form working devices the steps described previously in this chapter are usually not enough. *Doping*, the controlled addition of small quantities of an impurity to a material, is usually required to modify the electrical properties. Often the growth parameters that result in the desired crystal structure and composition do not yield the desired shape of the nanowire, in which case *etching* might be needed. Nanowire growth is very sensitive however and any addition to the growth process is likely to have more than one effect. The secondary effect of these processes on the nanowire crystal structure is discussed in section 4.1 and is the focus of paper II, and discussed in paper III in regards to doping, and in paper IV in regards to etching.

Doping

In the context of III-V semiconductors doping means replacing a few of the atoms with another element having fewer (an electron acceptor, p-type) or more (an electron donor,

n-type) valence electrons than the atom it replaces. This affects the type and availability of charge carriers in the material and is an essential part of turning nanowires into working devices. With nanowires it is desirable to add the dopants during growth in order to create sharp junctions and have a large degree of control over dopant distribution. In MOVPE growth this means introducing additional precursors during the growth. The amount of dopant that is desired varies a lot with the intended application, but concentrations of 10^{-19} cm^{-3} can be used as an example of the order of magnitude. This corresponds to replacing about 1 in 2000 atoms in the material with dopants. Using in-situ doping p-n junctions in GaAs were created already in the 90s.[60] In this case the dopants were Silane (n) and carbon from the group III precursors (p). Since then many more dopants have been evaluated for many different III-V combinations, see reference [61] for a comprehensive overview.

For InP examples of doping include Zn for p-doping (from diethyl zinc, DEZn[62]) and S for n-doping (from H_2S[63]). Both H_2S and DEZn, the dopants used in paper II and III, strongly affect the crystal structure of the resulting nanowire by inducing wurtzite and zincblende respectively. DEZn has a particularly dramatic effect and produces periodically twinned zincblende with $\{111\}$ sidefacets if introduced in high enough quantities.[62] In this case each twin segment is in the shape of a truncated octahedra giving the nanowires a "zig-zag" appearance when viewed from certain directions.[64] It is difficult to establish the mechanisms behind these effects as there are many parameters involved which might be affected by the introduction of new precursor species, such as surface passivation leading to changed surface diffusion lengths and surfactant effects which change the surface energies.

Another important aspect of doping which is interesting from a microanalysis point of view is their distribution. If for instance we are dealing with the (very) high dopant concentration of 10^{-19} cm^{-3} in a 20 nm wide nanowire there is only on average 3 or so dopant atoms present every nanometre. The doping could easily be a factor 10 or 100 lower, meaning that there will only be few dopant atoms present every 10 or 100 nm. If these atoms would tend to segregate to the nanowire surface, to twin planes or stacking faults or tend to aggregate this could have very large effects on the device. The low concentration of course makes any profiling of their distribution challenging. The best attempts at detection of dopants using electron microscopy involves heavy atoms in a Si matrix and have been performed using aberration corrected HAADF-STEM. In this way Au atoms originating from the gold particle have been located in nanowires,[65] and individual Sb dopant atoms have been imaged.[66] In both cases it was even possible to estimate how far down in the Si column the heavy atom was located.[67] Simulations indicate that this would not be possible using other high resolution methods.[66]

Another technique which deserves to be mentioned here is local electrode atom probe tomography (LEAP) where a small, tip-shaped sample is evaporated layer by layer allowing the atomic number to be determined for each leaving atom (or at least a sizeable fraction of them). Nanowires naturally fit the strict requirement of sample shape for this

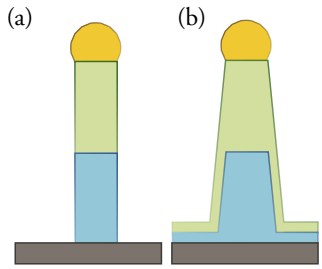

Figure 3.4: (a) Ideal axial heterostructure. (b) Axial heterostructure with unintentional radial growth which can bypass the heterojunction, reducing the performance of any device made from this nanowire.

technique. Using LEAP segregation of P in Ge nanowires have been observed with the core having a factor 10 lower and the shell a factor 10 higher concentration than the intended 10^{-19} cm^{-3}.[68] The same method has also been used to detected single gold atoms at concentrations of 100 ppm in InAs nanowires.[69] If dopant concentrations are greatly increased it might however be possible to measure their distributions using more conventional techniques, such as XEDS.

Etching

In the description of nanoparticle seeded nanowire growth in the previous section I suggested that under normal circumstances material is only incorporated under the gold particle. Although most of the material is indeed incorporated this way (otherwise no nanowires would form) there is in reality always some growth on the nanowire sidefacets in the radial direction, and directly on the substrate. Figure 3.4 illustrates the consequences this would have for an axial structure (this could be two different dopings or a heterostructure of two different materials). The material that is incorporated on the sides during the growth of the second material will form an unintentional shell around the entire nanowire making it tapered instead of straight. The radial growth then potentially forms a short circuit bypassing the junction in the middle, which would be hugely detrimental to the device. This could also be a problem for nanowires of a single material and doping; as mentioned earlier there is evidence that at least some dopants are incorporated at higher levels in the radially grown material compared to the axially grown material, resulting in an uneven dopant distribution. If this is the case also for MOVPE carbon incorporation even undoped nanowires of a single material would be affected.

Growth parameters can be adjusted to minimize this radial growth, but these might be fixed or limited due to other demands (e.g. the material will only grow under certain conditions, and only have the desired crystal structure under an even narrower set of pa-

rameters). *In-situ* etching introduces a reactive species during growth with the intention that it reacts preferably with material attached at undesired locations before it becomes fully incorporated into the nanowire (although this is not the only possible mechanism by which the etchants could hinder radial growth). For InP nanowire growth HCl has been successfully used for this purpose. It is important to note that the etchant needs to be introduced *during* growth in order to create untapered nanowires; only weakly adsorbed (physisorbed) In species on the sides are favorably removed. Once the material is fully incorporated into the structure (chemisorbed) the selectivity disappears. For this reason HCl etching post-growth does not reduce tapering.[70]

Chapter 4

Results

The effect on nanowire crystal structure for three important growth steps (p-doping with DEZn, n-doping with H_2S, and in-situ etching with HCl) were investigated using HRTEM. However, to determine the interface structure between the zincblende twins that are sometimes found in these types of nanowires, conventional HRTEM was not enough and a dual approach of negative C_3 imaging and focal series reconstruction was used. The effects of doping on the crystal structure could be determined (at full atomic resolution in the case of twin interfaces) but the cause of these changes are not known in detail, although a plausible mechanism for DEZn has been presented.

4.1 Changes in crystal structure with doping and etching

Doping with DEZn

Figure 4.1 shows TEM images of InP nanowires grown with DEZn molar fractions in the interval $0 - 1.1 \times 10^{-5}$. For comparison the group III (TMIn) fraction was 6.3×10^{-6} for all growths. From the high resolution images a trend towards zincblende with more and more regularly spaced twins can be seen. This is also visible in the overview TEM images for the two extreme cases where, in the case of high doping, the regular twinning produces a periodic striped pattern across the nanowire. Unlike dimethyl zinc (DMZn),[71] DEZn did not have any dramatic influence on the growth rate and the nanowires had roughly the same length independent of the dopant fraction.

In the highest doped nanowires Zn could reproducibly be detected by XEDS with quantifications showing around 0.5 atomic% (at such low levels quantifications must however be interpreted cautiously). Zn is known to incorporate at least partially through the gold particle,[63] but in this case no Zn could be detected in any of the gold particles. Many of the particles looked deformed and irregular, sometimes with pits on their surface (e.g. for 2.9×10^{-6} in figure 4.1). Possibly the composition which exists during

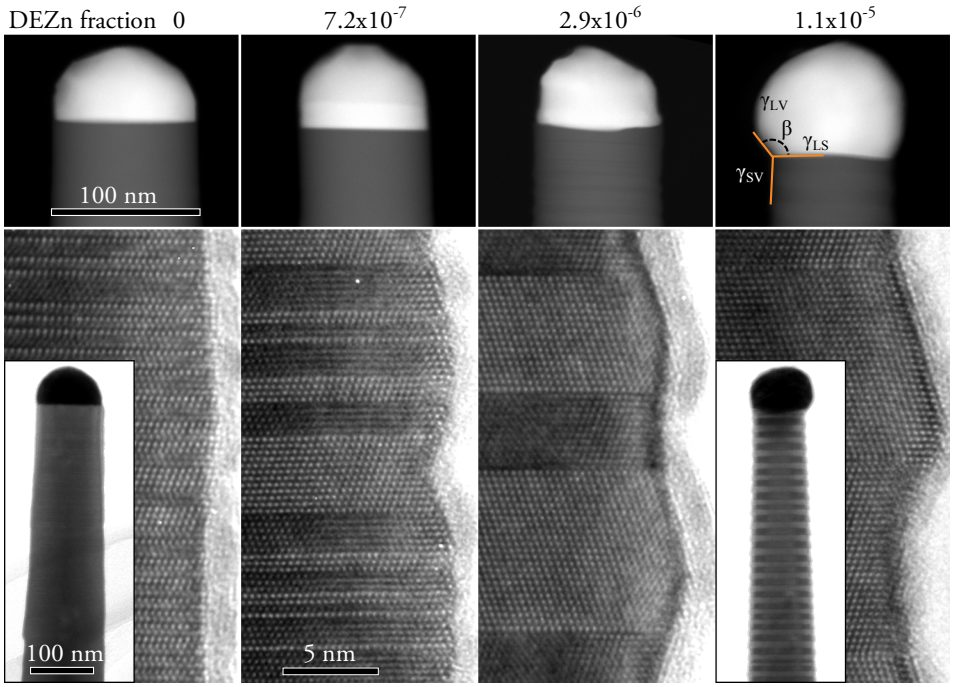

Figure 4.1: STEM image gold particle and top part of nanowire (top), and HRTEM image (bottom) showing the effect of DEZn doping on seed particle and crystal structure respectively. For the lowest and highest DEZn molar fractions a TEM overview image is also included to show the effects on morphology.

growth is not stable upon cool-down, which would account for both the lack of Zn and the deformed particles.

The distribution between zincblende and wurtzite (stacking faults and other structures which cannot be classified as either of the two make up at most a few %) is shown in figure 4.2 (a) as a function of DEZn fraction. At DEZn fractions of 2.9×10^{-6} the crystal structure is pure zincblende and a twinning superlattice has formed with fairly regular sized segments. Further increases of DEZn has two effects as seen in figure 4.2: increasing the average segment length and reducing the variation. The difference between the normal mixed crystal structure and twinning superlattices can be seen in a histogram of segment lengths, shown in figure 4.2 (b), where the former is monotonically decreasing while the latter has essentially zero occurrence of the shortest segment lengths.

In many models of polytypism in nanowires there are two main types of parameters: the supersaturation between the growth species in the particle and in the nanowire, $\Delta\mu$, and the surface energies, γ, between the liquid (L), vapour (V) and solid (S).

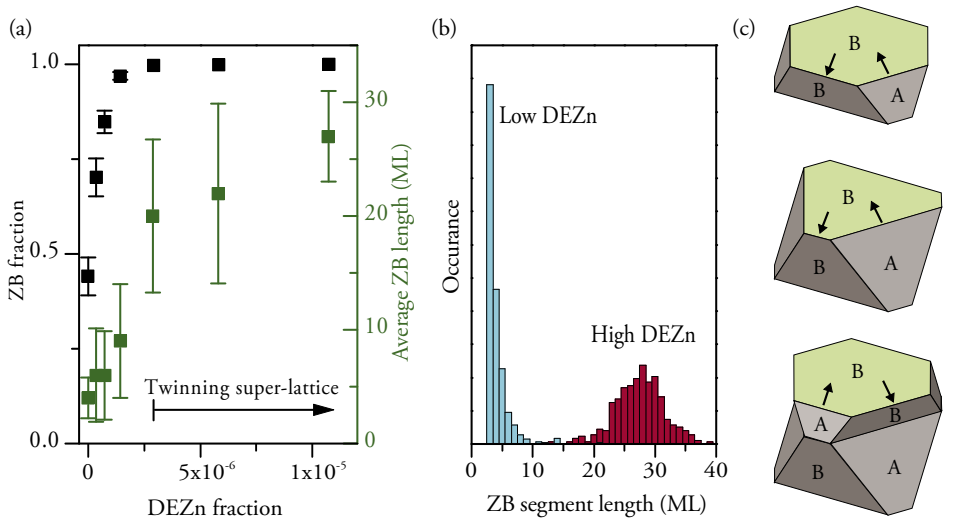

Figure 4.2: (a) Fraction of the nanowire which adopts the zincblende (ZB) structure and average length of the zincblende segments as a function of DEZn fraction. (b) Distribution of zincblende segment lengths for the case of an undoped nanowire and for high DEZn fractions where a twinning superlattice has formed. (c) Illustration of the changing nanowire cross-section during growth.

Growth rate gives a good indication of changes in supersaturation, but was not affected by DEZn as noted before. The γ_{LS}/γ_{LV} ratio will determine the contact angle, β, of the particle on the nanowire, but this is not measurable as the gold particle is deformed during cool-down. However for a constant particle volume the contact angle directly influences the diameter of the nanowire, allowing it to be measured (or at least compared between nanowires) reliably post-growth. The reduction in diameter with increasing DEZn (visible in the STEM images in figure 4.1, but quantified using SEM on several more nanowires) therefore indicate a reduced γ_{LS}/γ_{LV}. As discussed in section 3.2 this shifts the balance in favour of zincblende, since wurtzite formation is driven by having a lower $\gamma_{WZ,LS}$ than both the alternative $\gamma_{ZB,LS}$ and the γ_{LV} it replaces.

The formation of a twinning superlattice instead of a single zincblende crystal can be explained by the fact that the $\{111\}$ sidefacets are not parallel to the growth direction. With the addition of each new layer the cross-section becomes increasingly triangular as the $\{111\}$A facets grow and the $\{111\}$B shrink, shown in figure 4.2 (c). This deforms the particle up to a point where it is beneficial to form a nucleus with hexagonal stacking instead, and thus form a twin which will have a more hexagonal cross-section. With more DEZn the hexagonal nuclues becomes more unfavorable, requiring more distortion of the particle before forming and thus leading to longer segments.[62]

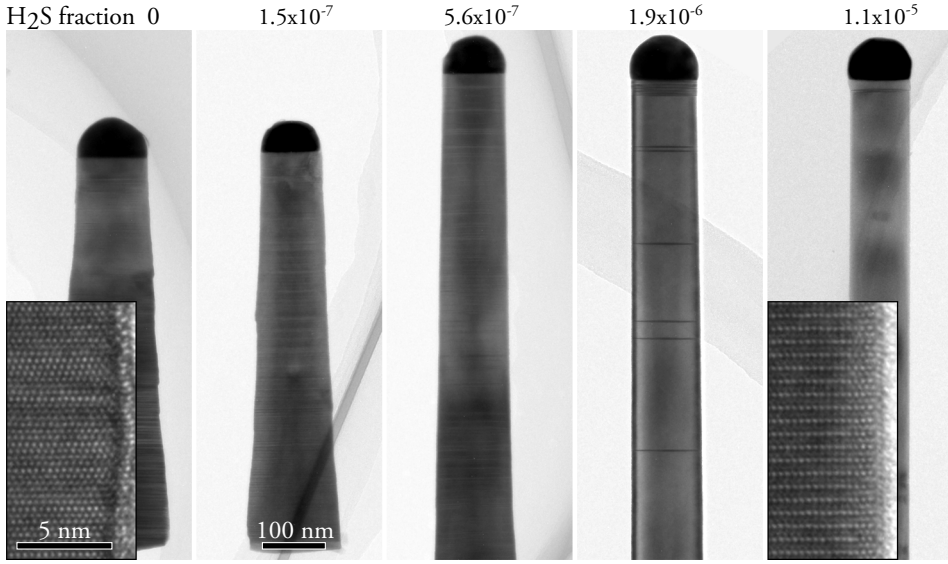

Figure 4.3: TEM overview images of nanowires from a H_2S doping series. For the undoped and highest doped nanowires a HRTEM inset shows the crystal structure. Stacking faults appear as lines across the structure, but at low doping they occur too frequently to provide much contrast in the images.

Doping with H_2S

Figure 4.3 shows TEM overview images of InP nanowires grown with varying H_2S molar fractions, but with otherwise identical conditions. The H_2S molar fractions used were between $0 - 1.1 \times 10^{-5}$. The inset HRTEM images show that the undoped nanowires have a mixed zincblende and wurtzite structure, while the highest doped nanowires are pure wurtzite. This change in crystal structure is also visible in the overview images as the stacking faults are visible as lines across the nanowire (however for the lowest doped nanowires they are so frequent that the contrast is very low).

Unlike the DEZn case the presence of H_2S during growth strongly increases the growth rate. S is a known surface passivator for InP[72] and will increase the surface diffusion length of the adsorbed precursors, and thus increase the amount of material available for axial growth. This increase in supersaturation is one factor that should favour the wurtzite structure. The surface passivation effect should also cause a reduction of radial growth which is visible as a reduced tapering of the nanowires at high H_2S molar fractions.

The maximum S content in the nanowires as measured by XEDS while illuminating the whole nanowire was around 1 atomic%. This is corresponds to a doping on the order of 3×10^{20} cm^{-3}. An example XEDS spectra of such a nanowire is shown in

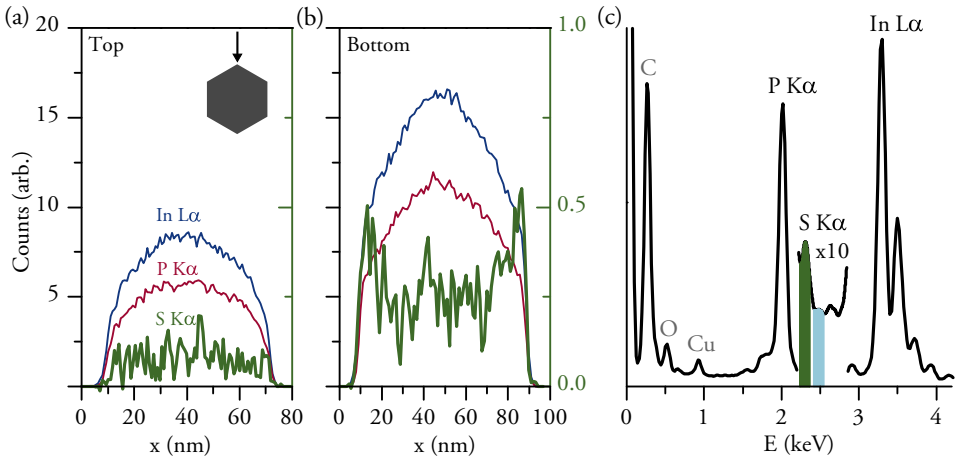

Figure 4.4: XEDS profiles across a highly S doped nanowire (a) close to the top, and (b) further towards the bottom. The latter case indicates a shell with higher doping than the core. (c) XEDS spectra from the bottom region showing the small S Kα peak riding on the tail of the much larger P Kα. To make the profiles in (a) and (b) the blue background was subtracted from the green S peak.

figure 4.4 (c), where a small S Kα peak can be seen riding on the tail of the much larger P Kα peak. In order to remove the effects of the P Kα background on the S profile a background, shown in blue, was subtracted.

In order to detect any radial variation of the S content XEDS line-scans were recorded across the nanowire close to its top and bottom. These two areas were separated by roughly 2 µm along the nanowire, but differed only about 20 nm in diameter. Since the potentially differently doped radial growth was quite thin and the spectra needed to be collected over long times to get measurable signals of S, it was important to minimize any beam damage. To accomplish this a spectrum image was first collected from a large area along the nanowire, and then summed in the axial direction to yield the profile. In this way the dose for each point in the radial profile is spread over a long distance along the nanowire. Similar spectrum acquisition schemes have been used for EELS.[73] The resulting radial profiles show (in a qualitative way) that close to the top the S concentration is too low to distinguish any variation from the noise, but close to the bottom there is a significant increase towards the edges. In contrast the In and P singal is monotonically decreasing, as is expected from the hexagonal cross section. This means there is a greater concentration of S in the radial growth than in the core, although the low signal prohibits any quantitative measure of this difference. Similar distributions of dopants have been seen for P in Ge nanowires using atom probe tomography.[68]

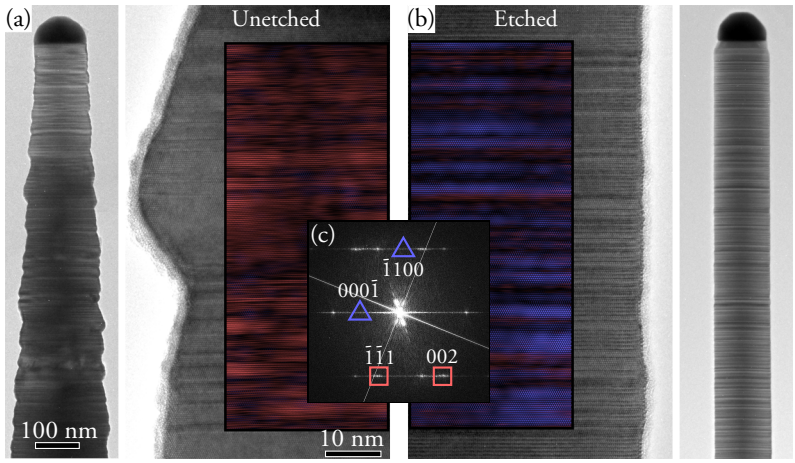

Figure 4.5: Overview TEM image showing morphology and HRTEM image showing crystal structure for (a) an unetched and (b) HCl ethced nanowire. The presence of HCl during growth clearly eliminates the unwanted radial growth. Color coding of zincblende (red) and wurtzite (blue) is provided by means of FFT filtering, illustrated in (c).

Etching with HCl

Figure 4.5 shows a TEM overview and a HRTEM image of an unetched reference nanowire (a), and (b) of a nanowire that was etched with HCl during growth. The HCl molar fraction was 3.3×10^{-5}, a factor 10 more than the molar fraction of the group III precursor. The introduction of the etchant improved the nanowire morphology dramatically as it essentially eliminated radial growth completely (which makes the etched nanowire completely untapered).

Fourier filtering using spots in the diffractogram characteristic for zincblende or wurtzite was used to highlight the change in crystal structure with etching. In figure 4.5 zincblende has been colored red and wurtzite blue to show the increase in wurtzite with HCl etching. The introduction of the very high HCl molar fractions required to eliminate radial growth makes it very complicated to find a single reason for the change in crystal structure, as this changes the precursor chemistry dramatically from the unetched case. Possibly there is an increase in supersaturation as species adsorbed to the sidefacets are chlorinated, making them available for axial growth instead of allowing them to incorporate as radial growth. The increase in growth rate which is then expected can in turn be masked by the fact that HCl also removes material from underneath the gold particle.[70] This decoupling of supersaturation from the (indirectly) observable growth rate further complicates the formulation of a mechanism for the crystal structure change.

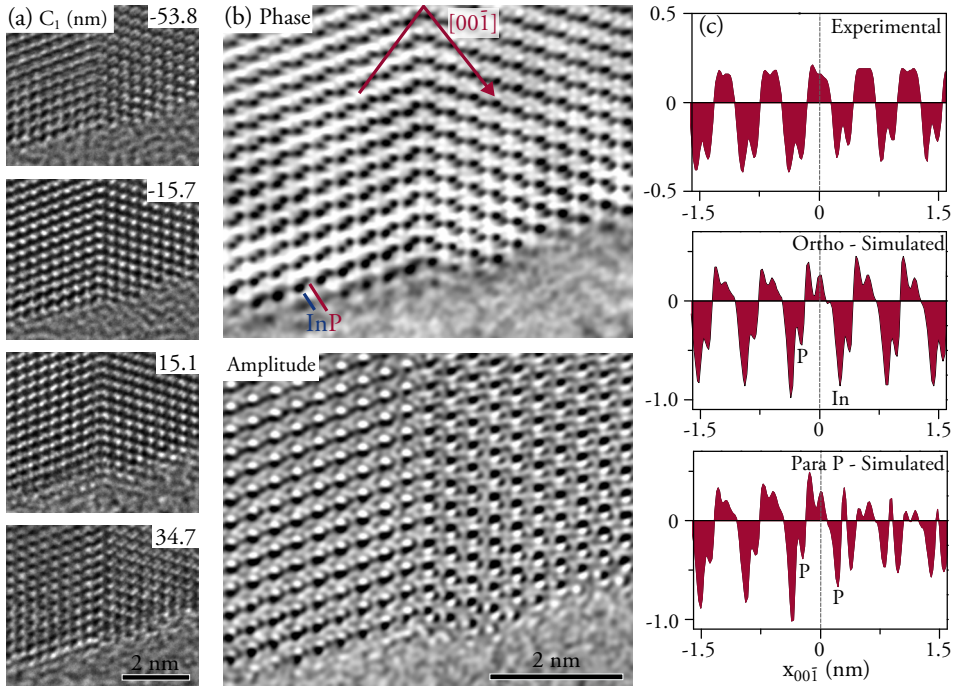

Figure 4.6: (a) 4 example HRTEM images from a 20 member focal series of an InP nanowire with a zincblende twinning superlattice, recorded with negative $C_3 = -10$ µm. (b) Reconstructed phase and amplitude of the object wavefunction using a linear Wiener filter method. The In-P dumbbells are clearly resolved and distinguishable. (c) Experimental and simulated phase line profiles in the dumbbell direction across the twin interface. The ortho model provides a much better match than the para-P model.

4.2 Twin interface structure

Even with hardware aberration correction and negative C_3, thickness is still a limiting factor for obtaining interpretable high resolution images. Figure 4.6 (a) shows 4 images from a 20 member focal series recorded with $C_3 = -10$ µm. Aberrations were measured by means of a Zemlin tableau recorded at 36 mrad, and corrected using the CEOS software. The other aberrations of importance were measured to: $|A_1| = 1.2$ nm, $|A_2| = 43$ nm, $|B_2| = 34$ nm and $C_5 = 1.8$ mm. This should yield a resolution of 0.12 nm, which is better than the 0.147 nm In-P dumbbell separation in a $\langle 110 \rangle$ projection.

At no defocus could the In-P atomic columns be resolved in such a way that they could be unambiguously distinguished, and therefor the interface structure could not be determined. This was verified by multislice simulations. In figure 4.6 (b) the re-

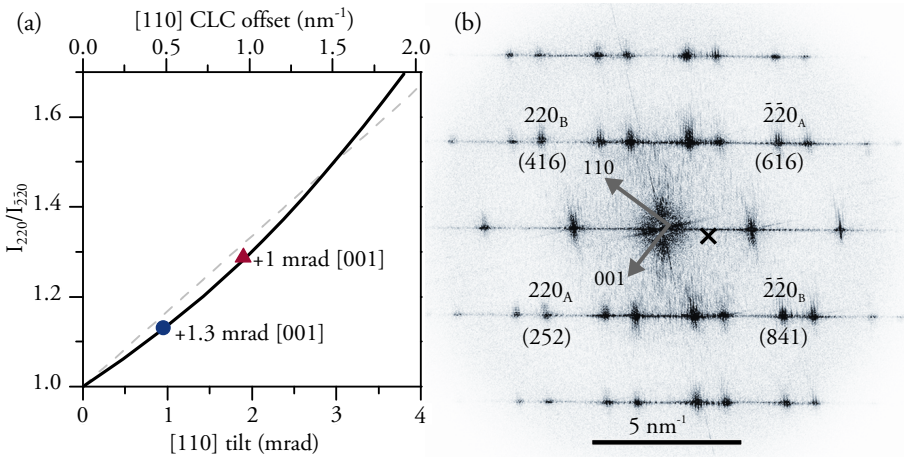

Figure 4.7: (a) Effects of crystal tilt in a [110] direction on the ratio of the two 220 type spot intensities (from multislice simulations). Two additional simulations which have tilts also in the perpendicular [001] direction show that the correlation of 220 intensity ratio and [110] tilt is robust. (b) Diffraction pattern calculated for the reconstructed object wavefunction with the centre of the Laue circle marked with "x", according to the method from (a).

constructed object wavefunction phase and amplitude is shown. The reconstruction corrected for the remaining aberrations due to the spherical aberration, defocus, and twofold astigmatism which had drifted a little and increased since the Zemlin tableu was recorded. Here the individual In and P columns can be resolved, displaying a contrast pattern where the leftmost atom of the pair is darker. Intuitively this can be interpreted as confirming the ortho model with In-P bonds across the interface. However looking more closely at the images in the focal series one can see a slight difference between the left and right twin segment, indicating that they are tilted slightly away from the intended $\langle 110 \rangle$ zone along non-equivalent directions. This could complicate the image interpretation.[74]

In order to estimate the nanowire misalignment the Fourier transform of the reconstructed object wavefunction was studied in detail. Unlike the conjugate symmetric diffractogram of a real-valued regular image, the Fourier transform of the object wavefunction is identical to the diffraction pattern and can be calculated from much smaller areas than can be obtained using a selected area aperture. In the diffraction pattern for thicker InP zincblende crystals $G \neq -G$ for most spots due to dynamical scattering, but exactly in the $\langle 110 \rangle$ zone the 220-type spots will have equal intensity. Any deviation from this is related to crystal tilt which results in unequal excitation errors for the two spots. The ratio of the intensity in the two spots, $I_{220}/I_{\bar{2}\bar{2}0}$, can therefore be related to

the crystal tilt in this particular direction as shown by figure 4.7.

Using the two non-parallel $\langle 220 \rangle$ directions from the two twin segments it was possible to estimate the magnitude and direction of the nanowire tilt away from the $\langle 110 \rangle$ zone. The centre of the Laue circle is marked in the calculated diffraction pattern in figure 4.7 (b) and corresponds to a 4 mrad tilt 3° away from the $[\bar{1}\bar{1}\bar{1}]$ direction. Using this estimate, phase profiles could be simulated along the dumbbell $[00\bar{1}]$ direction and compared to the experimental reconstruction, as shown in figure 4.6 (c). Clearly the ortho model provides the best match. Cross-sectional scanning tunneling microscopy has also found twins in GaAs nanowires to be of the ortho type.[75] For InAs, aberration corrected STEM has been used for the same purpose.[76]

It is important to note that the experimental profile showed the same qualitative agreement with the ortho model also when using tilt magnitudes ± 1.5 mrad and directions $\pm 20°$ from the estimate. For tilt directions 180° away from the estimate the difference between the In and P columns disappeared, which shows the importance of knowing the precise crystal alignment.

4.3 Outlook

Heterostructures are particularly interesting materials for beyond-HRTEM methods, in my opinion. If the atomic columns can be fully resolved at the interface, and the contrast of the columns be accurately related to composition, it would be possible to map transitions with very high spatial resolution. For heterostructures where both group III and group V are switched it might be possible using these methods to tell if one or the other switches a few bilayers earlier, or if one switch occurs more sharply than the other. This is of course important information both for analysing the nanowire's performance in devices, and in order to understand the growth.[38]

These high resolution images do not need to come from TEM: aberration corrected STEM could provide the same or better resolution while at the same time be less sensitive to small tilts and varying thickness compared to aberration corrected TEM or image series reconstructions. In addition, the HAADF signal can under some conditions be directly related to composition.[77] Recent developments in XEDS also allow chemical mapping at atomic resolution.[78]

For finding directions (as is the case for paper I in this thesis) rather than compositions, convergent beam electron diffraction (CBED) is an interesting option. If the difference in Z between group III and group V is large one can use dynamical diffraction effects from thicker samples to differentiate G and $-G$ (e.g. GaN[79]). If instead it is very small, one can use a phase differences between different scattering pathways for the same purpose (e.g. GaAs[80]). In these cases CBED might be a considerably easier method, both for acquiring and interpreting the images.

There is no lack of options for electron microscopy techniques that could be useful for nanowires!

Acknowledgements

There are enough people whom I should thank to fill another chapter, but I'll try to keep it short:

I would of course like to thank my supervisors, Reine and Kimberly, for all the support and help, and for making it possible to call recording images of atoms "work".

For the practical TEM work Lisa gave me a head start in many different areas; I am very grateful for the week of full-time tutoring. Also many thanks to Crispin for your part of the focal series work and for keeping me on my toes regarding knowledge of the microscopes. To Gunnel for making sure the equipment actually works. I have enjoyed our soldering sessions very much.

At FTF I would like to give special thanks to Magnus and Jesper for giving me the opportunity to take part in so many interesting projects, and for providing me with the material I needed for my own (which was not exactly easy to find in the archives).

Apart from these projects I have also had the pleasure of working with many more from FTF: Mattias, Jessica, Anders, Jonas, and Magnus H. Then there are all the other people at FTF with whom I have had many a discussion about TEM and nanowires, who have been excellent travelling partners to conferences, who have helped out at the TEM when the organic chemists have made glögg etc.: Maria, Karla, Sebastian and Daniel. Huge thanks to you all!

At Polymer & Materials Chemistry there are also my fellow PhD students who have helped making the past 2.5 years fun and interesting: Elin, Anna, Shogo, Isa, Carola, Annika, Carlos, and my fellow microscopist Filip.

Last but not least: friends, family and sambos. Thanks for all the support!

References

[1] M. W. Larsson, J. B. Wagner, M. Wallin, P. Håkansson, L. E. Fröberg, L. Samuelson, and L. R. Wallenberg, "Strain mapping in free-standing heterostructured wurtzite InAs/InP nanowires", *Nanotechnology* **18** (2007) 015504

[2] P. Caroff, M. E. Messing, B. M. Borg, K. A. Dick, K. Deppert, and L.-E. Wernersson, "InSb heterostructure nanowires: MOVPE growth under extreme lattice mismatch.", *Nanotechnology* **20** (2009) 495606

[3] M. T. Björk, B. J. Ohlsson, C. Thelander, A. I. Persson, K. Deppert, L. R. Wallenberg, and L. Samuelson, "Nanowire resonant tunneling diodes", *Applied Physics Letters* **81** (2002) 4458–4460

[4] J. Wallentin, J. M. Persson, J. B. Wagner, L. Samuelson, K. Deppert, and M. T. Borgström, "High-performance single nanowire tunnel diodes.", *Nano letters* **10** (2010) 974–9

[5] B. M. Borg, K. A. Dick, B. Ganjipour, M.-E. Pistol, L.-E. Wernersson, and C. Thelander, "InAs/GaSb Heterostructure Nanowires for Tunnel Field-Effect Transistors.", *Nano letters* **10** (2010) 4080–4085

[6] C. Thelander, T. Mårtensson, M. T. Björk, B. J. Ohlsson, M. W. Larsson, L. R. Wallenberg, and L. Samuelson, "Single-electron transistors in heterostructure nanowires", *Applied Physics Letters* **83** (2003) 2052–2054

[7] T. Mårtensson, C. P. T. Svensson, B. A. Wacaser, M. W. Larsson, W. Seifert, K. Deppert, A. Gustafsson, L. R. Wallenberg, and L. Samuelson, "Epitaxial III-V Nanowires on Silicon", *Nano Letters* **4** (2004) 1987–1990

[8] E. P. A. M. Bakkers, M. T. Borgström, and M. A. Verheijen, "Epitaxial Growth of III-V Nanowires on Group IV Substrates", *MRS Bulletin* **32** (2007) 14–19

[9] M. D. Schroer and J. R. Petta, "Correlating the nanostructure and electronic properties of InAs nanowires.", *Nano letters* **10** (2010) 1618–22

[10] C. Thelander, P. Caroff, S. Plissard, A. W. Dey, and K. A. Dick, "Effects of Crystal Phase Mixing on the Electrical Properties of InAs Nanowires.", *Nano letters* **11** (2011) 2424–2429

[11] P. Caroff, K. A. Dick, J. Johansson, K. Deppert, M. E. Messing, and L. Samuelson, "Controlled polytypic and twin-plane superlattices in III-V nanowires", *Nature Nanotechnology* **4** (2009) 50–55

[12] J. Bolinsson, P. Caroff, B. Mandl, and K. A. Dick, "Wurtzite-zincblende superlattices in InAs nanowires using a supply interruption method.", *Nanotechnology* **22** (2011) 265606

[13] M. A. O'Keefe, "Seeing atoms with aberration-corrected sub-Ångström electron microscopy", *Ultramicroscopy* **108** (2008) 196–209

[14] D. B. Williams and C. B. Carter, *Transmission Electron Microscopy: A Textbook for Materials Science*, Springer, New York, 2 edition (2009)

[15] R. R. Meyer, A. I. Kirkland, R. E. Dunin-Borkowski, and J. L. Hutchison, "Experimental characterisation of CCD cameras for HREM at 300 kV", *Ultramicroscopy* **85** (2000) 9–13

[16] S. Haigh, *Super Resolution Tilt Series Exit Wave Restoration from Aberration Corrected Images*, Ph.D. thesis, Oxford University (2008)

[17] M. A. O'Keefe, ""Resolution" in high-resolution electron microscopy", *Ultramicroscopy* **47** (1992) 282–297

[18] A. I. Kirkland and R. R. Meyer, ""Indirect" High-Resolution Transmission Electron Microscopy: Aberration Measurement and Wavefunction Reconstruction", *Microscopy and Microanalysis* **10** (2004) 401–413

[19] P. W. Hawkes, "Aberration correction past and present.", *Philosophical transactions of the Royal Society A* **367** (2009) 3637–64

[20] A. F. de Jong and D. Van Dyck, "Ultimate resolution and information in electron microscopy II. The information limit of transmission electron microscopes", *Ultramicroscopy* **49** (1993) 66–80

[21] M. Lentzen, "Progress in Aberration-Corrected High-Resolution Transmission Electron Microscopy Using Hardware Aberration Correction", *Microscopy and Microanalysis* **12** (2006) 191

[22] A. I. Kirkland, R. R. Meyer, and L.-Y. S. Chang, "Local Measurement and Computational Refinement of Aberrations for HRTEM", *Microscopy and Microanalysis* **12** (2006) 461

[23] F. Zemlin, K. Weiss, P. Schiske, and W. Kunath, "Coma-free alignment of high resolution electron microscopes with the aid of optical diffractograms", *Ultramicroscopy* **3** (1978) 49–60

[24] J. L. Hutchison, J. M. Titchmarsh, D. J. H. Cockayne, R. C. Doole, C. J. D. Hetherington, A. I. Kirkland, and H. Sawada, "A versatile double aberration-corrected, energy filtered HREM/STEM for materials science.", *Ultramicroscopy* **103** (2005) 7–15

[25] R. R. Meyer, A. I. Kirkland, and W. O. Saxton, "A new method for the determination of the wave aberration function for high resolution TEM 1. Measurement of the symmetric aberrations", *Ultramicroscopy* **92** (2002) 89–109

[26] M. Haider, S. Uhlemann, E. Schwan, H. Rose, B. Kabius, and K. W. Urban, "Electron microscopy image enhanced", *Nature* **392** (1998) 768–769

[27] L. Y. Chang, F. R. Chen, A. I. Kirkland, and J. J. Kai, "Calculations of spherical aberration-corrected imaging behaviour", *Journal of Electron Microscopy* **52** (2003) 359–364

[28] M. Lentzen, B. Jahnen, C.-L. Jia, A. Thust, K. Tillmann, and K. Urban, "High-resolution imaging with an aberration-corrected transmission electron microscope.", *Ultramicroscopy* **92** (2002) 233–42

[29] C.-L. Jia, M. Lentzen, and K. W. Urban, "High-Resolution Transmission Electron Microscopy Using Negative Spherical Aberration", *Microscopy and Microanalysis* **10** (2004) 174–184

[30] C.-L. Jia, M. Lentzen, and K. Urban, "Atomic-resolution imaging of oxygen in perovskite ceramics.", *Science* **299** (2003) 870–3

[31] K. W. Urban, "Studying atomic structures by aberration-corrected transmission electron microscopy.", *Science* **321** (2008) 506–510

[32] L.-Y. Chang and A. I. Kirkland, "Comparisons of Linear and Nonlinear Image Restoration", *Microscopy and Microanalysis* (2006) 469–475

[33] A. Thust, W. M. J. Coene, M. Op De Beeck, and D. Van Dyck, "Focal-series reconstruction in HRTEM: simulation studies on non-periodic objects", *Ultramicroscopy* **64** (1996) 211–230

[34] W. O. Saxton, "What is the focus variation method? Is it new? Is it direct?", *Ultramicroscopy* **55** (1994) 171–181

[35] R. R. Meyer, A. I. Kirkland, and W. O. Saxton, "A new method for the determination of the wave aberration function for high-resolution TEM. 2. Measurement of the antisymmetric aberrations", *Ultramicroscopy* **99** (2004) 115–123

[36] X. Xu, S. P. Beckman, P. Specht, E. R. Weber, D. C. Chrzan, R. P. Erni, I. Arslan, N. Browning, A. Bleloch, and C. Kisielowski, "Distortion and Segregation in a Dislocation Core Region at Atomic Resolution", *Physical Review Letters* **95** (2005) 145501

[37] K. Tillmann, K. W. Urban, and A. Thust, "Spherical Aberration Correction in Tandem with Exit-Plane Wave Function Reconstruction: Interlocking Tools for the Atomic Scale Imaging of Lattice Defects in GaAs", *Microscopy and Microanalysis* **10** (2004) 185–198

[38] K. Mahalingam, K. G. Eyink, G. J. Brown, D. L. Dorsey, C. F. Kisielowski, and A. Thust, "Compositional analysis of mixed-cation-anion III-V semiconductor interfaces using phase retrieval high-resolution transmission electron microscopy.", *Journal of microscopy* **230** (2008) 372–81

[39] K. Ishizuka, "FFT multislice method–the silver anniversary.", *Microscopy and Microanalysis* **10** (2004) 34–40

[40] M. J. Hÿtch and W. M. Stobbs, "Quantitative comparison of high resolution TEM images with image simulations", *Ultramicroscopy* **53** (1994) 191–203

[41] A. Thust, "High-Resolution Transmission Electron Microscopy on an Absolute Contrast Scale", *Physical Review Letters* **102** (2009) 5–8

[42] C. B. Boothroyd, "Why don't high-resolution simulations and images match?", *Journal of Microscopy* **190** (1998) 99–108

[43] D. Van Dyck, "Persistent misconceptions about incoherence in electron microscopy.", *Ultramicroscopy* **111** (2011) 894–900

[44] J. J. Friel and C. E. Lyman, "X-ray mapping in electron-beam instruments.", *Microscopy and microanalysis* **12** (2006) 2–25

[45] D. B. Williams, J. Michael, J. I. Goldstein, and A. D. Romig Jr., "Definition of the spatial resolution of X-ray microanalysis in thin foils", *Ultramicroscopy* **47** (1992) 121–132

[46] D. L. Smith, *Thin-Film Deposition: Principles and Practice*, McGraw Hill, New York (1995)

[47] B. Mandl, J. Stang, T. Mårtensson, A. Mikkelsen, L. S. Karlsson, J. Eriksson, G. Bauer, L. Samuelson, and W. Seifert, "Au-Free Epitaxial Growth of InAs Nanowires", *Nano Letters* **6** (2006) 1817–1821

[48] M. Messing, K. Hillerich, J. Johansson, K. Deppert, and K. Dick, "The use of gold for fabrication of nanowire structures", *Gold Bulletin* **42** (2009) 172–181

[49] D. Kriegner, C. Panse, B. Mandl, K. A. Dick, M. Keplinger, J. M. Persson, P. Caroff, D. Ercolani, L. Sorba, F. Bechstedt, J. Stangl, and G. Bauer, "Unit cell structure of crystal polytypes in InAs and InSb nanowires.", *Nano letters* **11** (2011) 1483–9

[50] V. G. Dubrovskii and N. V. Sibirev, "Growth thermodynamics of nanowires and its application to polytypism of zinc blende III-V nanowires", *Physical Review B* **77** (2008) 035414

[51] D. B. Holt, "Grain boundaries in the sphalerite structure", *Journal of Physics and Chemistry of Solids* **25** (1964) 1385–1395

[52] D. B. Holt, "Polarity reversal and symmetry in semiconducting compounds with the sphalerite and wurtzite structures", *Journal of Materials Science* **19** (1984) 439–446

[53] C. Yeh, Z. Lu, S. Froyen, and A. Zunger, "Zinc-blende-wurtzite polytypism in semiconductors", *Physical Review B* **46** (1992) 10086

[54] R. Leitsmann and F. Bechstedt, "Surface influence on stability and structure of hexagon-shaped III-V semiconductor nanorods", *Journal of Applied Physics* **102** (2007) 063528

[55] T. Akiyama, K. Sano, K. Nakamura, and T. Ito, "An Empirical Potential Approach to Wurtzite-Zinc-Blende Polytypism in Group III-V Semiconductor Nanowires", *Japanese Journal of Applied Physics* **45** (2006) L275–L278

[56] J. Johansson, K. A. Dick, P. Caroff, M. E. Messing, J. Bolinsson, K. Deppert, and L. Samuelson, "Diameter dependence of the wurtzite-zinc blende transition in InAs nanowires", *Journal of Physical Chemistry C* **114** (2010) 3837–3842

[57] J. Johansson, L. S. Karlsson, C. P. T. Svensson, B. A. Wacaser, T. Mårtensson, K. Deppert, L. Samuelson, and W. Seifert, "Structural properties of <111>B - oriented III-V nanowires.", *Nature materials* **5** (2006) 574–80

[58] F. Glas, J.-C. Harmand, and G. Patriarche, "Why Does Wurtzite Form in Nanowires of III-V Zinc Blende Semiconductors?", *Physical Review Letters* **99** (2007) 146101

[59] H. J. Joyce, J. Wong-Leung, Q. Gao, H. H. Tan, and C. Jagadish, "Phase perfection in zinc Blende and Wurtzite III-V nanowires using basic growth parameters.", *Nano letters* **10** (2010) 908–15

[60] K. Haraguchi, T. Katsuyama, K. Hiruma, and K. Ogawa, "GaAs p-n junction formed in quantum wire crystals", *Applied Physics Letters* **60** (1992) 745–747

[61] J. Wallentin, *Doping of semiconductor nanowires*, Licentiate thesis, Lund University (2011)

[62] R. E. Algra, M. A. Verheijen, M. T. Borgström, L.-F. Feiner, G. Immink, W. J. P. Van Enckevort, E. Vlieg, and E. P. A. M. Bakkers, "Twinning superlattices in indium phosphide nanowires.", *Nature* **456** (2008) 369–72

[63] M. H. M. van Weert, A. Helman, W. van Den Einden, R. E. Algra, M. A. Verheijen, M. T. Borgström, G. Immink, J. J. Kelly, L. P. Kouwenhoven, and E. P. A. M. Bakkers, "Zinc incorporation via the vapor-liquid-solid mechanism into InP nanowires.", *Journal of the American Chemical Society* **131** (2009) 4578–9

[64] L. S. Karlsson, K. A. Dick, J. B. Wagner, J.-O. Malm, K. Deppert, L. Samuelson, and L. R. Wallenberg, "Understanding the 3D structure of GaAs <111> B nanowires", *Nanotechnology* **18** (2007) 485717

[65] J. Allen, E. Hemesath, D. Perea, J. Lensch-Falk, Z. Li, F. Yin, M. Gass, P. Wang, A. Bleloch, R. Palmer, and L. J. Lauhon, "High-resolution detection of Au catalyst atoms in Si nanowires", *Nature Nanotechnology* **3** (2008) 168–173

[66] P. M. Voyles, D. A. Muller, J. L. Grazul, P. H. Citrin, and H.-J. L. Gossmann, "Atomic-scale imaging of individual dopant atoms and clusters in highly n-type bulk Si.", *Nature* **416** (2002) 826–9

[67] D. A. Muller, P. M. Voyles, and E. J. Kirkland, "Depth-dependent imaging of individual dopant atoms in silicon.", *Microscopy and Microanalysis* **10** (2004) 291–300

[68] D. E. Perea, E. R. Hemesath, E. J. Schwalbach, J. L. Lensch-falk, P. W. Voorhees, and L. J. Lauhon, "Direct measurement of dopant distribution in an individual vapour-liquid-solid nanowire", *Nature Nanotechnology* **4** (2009) 315–319

[69] D. E. Perea, J. E. Allen, J. S. May, B. W. Wessels, D. N. Seidman, and L. J. Lauhon, "Three-dimensional nanoscale composition mapping of semiconductor nanowires", *Nano Lett.* **6** (2006) 181–185

[70] M. T. Borgström, J. Wallentin, K. Kawaguchi, L. Samuelson, and K. Deppert, "Dynamics of extremely anisotropic etching of InP nanowires by HCl", *Chemical Physics Letters* **502** (2011) 222–224

[71] M. T. Borgström, E. Norberg, P. Wickert, H. a. Nilsson, J. Trägårdh, K. A. Dick, G. Statkute, K. Deppert, P. Ramvall, and L. Samuelson, "Precursor evaluation for in situ InP nanowire doping", *Nanotechnology* **19** (2008) 445602

[72] H.-L. Lu, Y. Terada, Y. Shimogaki, Y. Nakano, and M. Sugiyama, "In situ passivation of InP surface using H_2S during metal organic vapor phase epitaxy", *Applied Physics Letters* **95** (2009) 152103

[73] K. Sader, B. Schaffer, G. Vaughan, R. Brydson, A. Brown, and A. Bleloch, "Smart acquisition EELS", *Ultramicroscopy* **110** (2010) 998–1003

[74] C. J. D. Hetherington, "HREM of defects in silicon at twin intersections", *Materials Research Society Symposium Proceedings* **183** (1990) 123–134

[75] A. Mikkelsen, L. Ouattara, J. N. Andersen, L. Samuelson, W. Seifert, and E. Lundgren, "Direct imaging of the atomic structure inside a nanowire by scanning tunnelling microscopy", *Nature Materials* **3** (2004) 519–523

[76] P. Krogstrup, J. Yamasaki, C. B. Sørensen, E. Johnson, J. B. Wagner, R. Pennington, M. Aagesen, N. Tanaka, and J. Nygård, "Junctions in axial III-V heterostructure nanowires obtained via an interchange of group III elements.", *Nano letters* **9** (2009) 3689–93

[77] T. Volkenandt, E. Müller, D. Z. Hu, D. M. Schaadt, and D. Gerthsen, "Quantification of sample thickness and in-concentration of InGaAs quantum wells by transmission measurements in a scanning electron microscope.", *Microscopy and Microanalysis* **16** (2010) 604–13

[78] A. J. D'Alfonso, B. Freitag, D. Klenov, and L. J. Allen, "Atomic-resolution chemical mapping using energy-dispersive x-ray spectroscopy", *Physical Review B* **81** (2010) 100101(R)

[79] F. A. Ponce, D. P. Bour, W. T. Young, M. Saunders, and J. W. Steeds, "Determination of lattice polarity for growth of GaN bulk single crystals and epitaxial layers", *Applied Physics Letters* **69** (1996) 337–339

[80] J. Taftø and J. C. H. Spence, "A simple method for the determination of structure-factor phase relationships and crystal polarity using electron diffraction", *Journal of Applied Crystallography* **15** (1982) 60–64